Production Processes as a Tool to Study Parameterizations of Quark Confinement

S. Ahlig, R. Alkofer[*], C. Fischer, M. Oettel[†], H. Reinhardt, and H. Weigel[‡]

Institute for Theoretical Physics, University of Tübingen
Auf der Morgenstelle 14, D-72076 Tübingen, Germany
(February 1, 2008)

Abstract

We introduce diquarks as separable correlations in the two–quark Green's function to facilitate the description of baryons as relativistic three–quark bound states. These states then emerge as solutions of Bethe–Salpeter equations for quarks and diquarks that interact via quark exchange. When solving these equations we consider various dressing functions for the free quark and diquark propagators that prohibit the existence of corresponding asymptotic states and thus effectively parameterize confinement. We study the implications of qualitatively different dressing functions on the model predictions for the masses of the octet baryons as well as the electromagnetic and strong form factors of the nucleon. For different dressing functions we in particular compare the predictions for kaon photoproduction, $\gamma p \to K\Lambda$, and associated strangeness production, $pp \to pK\Lambda$, with experimental data. This leads to conclusions on the permissibility of different dressing functions.

---

[*]E-Mail: reinhard.alkofer@uni-tuebingen.de

[†]Address after Feb. 1st, 2001: CSSM, University of Adelaide, SA 5005, Australia

[‡]Heisenberg–Fellow

I. INTRODUCTION

The complexity of Quantum Chromodynamics (QCD) inhibits the computation of hadronic properties and reactions from first principles. As a consequence models that potentially imitate the essentials of the QCD dynamics have been developed in the past to describe hadrons. A relativistic description of baryons as three–quark bound states is provided by the solutions of the Bethe–Salpeter equations[1] for quarks and diquarks which interact via quark exchange [3–5]. Once the full three–quark problem has been reduced to an effective two–body problem, the only model ingredients are the (di)quark propagators along with the quark–diquark vertices. It is hoped for that further progress in the study of the QCD quark propagator and two–quark correlations will eventually justify the reduction to quarks and diquarks in this approach to describe baryons.

Actual calculations utilize either simplifying assumptions or phenomenological parameterizations of the respective propagators and interaction vertices of quarks and diquarks. By choosing the simplest *ansätze*, *i.e.* free spin–1/2 and spin–0/spin–1 propagators for quarks and diquarks, respectively, various spacelike nucleon form factors have been successfully reproduced [6]. However, the naïve use of perturbative (di)quark propagators leads to asymptotic states in the spectrum that carry the respective quantum numbers. Hence baryons would decay into quarks unless kinematically bound. This decay process would contradict the confinement phenomenon. In this paper we will therefore investigate the possibility of incorporating confinement into the diquark model by suitable modifications of the quark and diquark propagators. Essentially these propagators are modified by multiplicative dressing functions to completely remove the poles that occurred in the perturbative propagators at the (di)quark masses. This enables us to calculate the spectrum not only of octet but also decuplet baryons [7]. Together with an *ansatz* for the quark–diquark bound state wave–function of the nucleon (Faddeev amplitude) such pole–free propagators have already been used to calculate nucleon form factors in the spacelike regime [8,9]. Unfortunately in this context the computation of the electro–weak form factors is not as simple as merely modifying the propagators. Since gauge invariance relates off–shell propagators and vertices it is obvious that any change in the propagators requires modifications of the effective interaction with the electro–weak gauge bosons [10]. When incorporating gauge invariance in the model with free propagators the nucleon isovector magnetic moments come out too small by about 30% unless model parameters are used that do not properly reproduce the baryon spectrum [6]. However, these unacceptable parameters result from requiring the Δ–isobar to be kinematically bound against its decay into free quarks. It is hoped for that when modeling confinement the results on the magnetic moments will also improve due to the modifications of the photon vertices which are mandatory when employing dressed (di)quark propagators. A very serious disadvantage of the lack of confinement is that hadronic reactions with *timelike* momenta of the order of 1GeV transferred to the nucleon, *e.g.* meson production processes, cannot be described properly. Again, the free–particle poles of quark and diquark cause unphysical thresholds in these processes that are triggered by the poles in the

---

[1]For further details on the application of the Bethe–Salpeter formalism to QCD we refer to reviews [1,2] and references therein.

propagators. An appropriate modification of these propagators would not only remove the unphysical thresholds but also serve as an effective description of the strong interaction. Certainly, a relativistic description of such processes would be very desirable. At present, the covariant diquark model appears to be the only relativistic one that is both, feasible and applicable at this energy scale.

As already mentioned we wish to eliminate the singularities associated with real timelike momenta in the (di)quark propagators that would lead to imaginary parts in those S–matrix elements that are calculated from diagrams containing internal quark loops. So, either these singularities are absent or their contributions cancel in some manner [2]. The qualitative behavior described can be encoded in the following models (which are certainly not the only possibilities) for the quark propagator in Euclidean space,

$$S^{(k)}(p) = \frac{i\not{p} - m_q}{p^2 + m_q^2} \, f_k\left(\frac{p^2}{m_q^2}\right) \, , \qquad k = 0, \ldots, 3 \, , \tag{1}$$

with

$$f_0(x) = 1 \qquad \qquad \text{(bare propagator)} \, , \tag{2}$$

$$f_1(x) = \frac{1}{2}\left\{ \frac{x+1}{x+1-i/d} + \frac{x+1}{x+1+i/d} \right\} \, , \tag{3}$$

$$f_2(x) = 1 - \exp\left[-d\,(1+x)\right] \, , \tag{4}$$

$$f_3(x, x^*) = \tanh\left[d\,(1+x)\,(1+x^*)\right] \, . \tag{5}$$

The propagator (3) possesses complex conjugate poles [11] such that corresponding virtual excitations cancel each other in physical amplitudes. Here m represents a parameter that would be interpreted as the quark mass if and only if the poles were on the real axis. In another scenario (4), the dressing functions are chosen such that the propagators are entire functions and non–trivial in the whole complex plane [12,9]. If they are required to be analytic, they must possess an essential singularity, at least for infinite arguments. Third, it might be helpful to approximate propagators by non–analytic functions (5) and constrain them such that they asymptotically behave like $1/|p|^2$ for both, large spacelike and timelike momenta. Since we enforce the propagators to be free of poles, they must be non–analytic functions depending on both the particle momentum p and its complex conjugate p^*. Consequently the quark–photon and quark–meson vertices are non–analytic and, even worse, translation invariance is lost in the solutions to the nucleon Bethe–Salpeter equation. These issues will be detailed in section II. The trivial dressing function f_0 corresponds to the bare propagator. We will consider this case only for comparison.

In figure 1 we show $\tilde{f}_k(x) = f_k(x)/(x+1)$ for $k = 0, \ldots, 3$ for real x. Note that these dressing functions are real in that case. We observe that $\tilde{f}_1(x)$ and $\tilde{f}_3(x)$ change sign (as in the case of a tree–level propagator) while the function $\tilde{f}_2(x)$ increases drastically. For asymptotically large spacelike momenta the three model propagators $S^{(k)}$, ($k = 1, 2, 3$) match up with the bare propagator $S^{(0)}$. Our present investigation focuses on the phenomenological implications of the so–modified propagators.

This paper is organized as follows: In Section II the covariant diquark model for baryons is presented. The corresponding Bethe–Salpeter equation that describes baryons as bound states of quarks and diquarks is derived in appendix A. The formalism of refs. [13,6] for
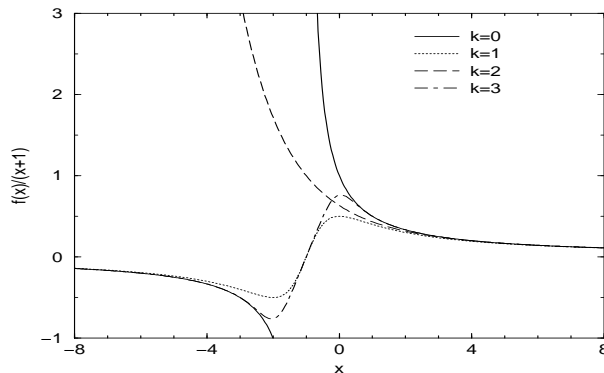
FIG. 1. The propagator functions, $\tilde{f}_k(x) = f_k(x)/(x+1)$ for real x and for $k = 0, \ldots, 3$, cf. eqs (2)–(5). The thick solid line corresponds to the free propagator. Here we have set $d = 1$.

calculating form factors is described for later determination of model parameters. Using the above given scenarios for implementing the confinement phenomena at the level of propagators this will set the stage for the main topic of our paper: The sensitivity of the predicted observables on the various effective parameterizations of confinement. These parameterizations concern the structure of the (di)quark propagators for complex momenta. In section III we will discuss the regime of complex momenta that is relevant for studying the baryon spectrum as well as several production processes. In section IV we will describe the formalism necessary to compute various production processes in the diquark–quark model. These comprise especially the cross sections for kaon photoproduction $p\gamma \to K\Lambda$ and the associated strangeness production in $pp \to pK\Lambda$. We will proceed by presenting our numerical results in section V, including the determination of the model parameters. In particular we will compare the predictions that originate from the different dressing functions for the propagators. Finally, we will conclude by formulating criteria for phenomenologically permissible parameterizations of the propagators. Some derivations and technical details are relegated to four appendices.

II. THE COVARIANT DIQUARK MODEL FOR BARYONS

A. The diquark–quark Bethe–Salpeter equation

We start from the Faddeev formalism for three quarks and impose two essential assumptions to arrive at a Bethe–Salpeter equation that describes baryons as bound states of quarks and diquarks interacting via quark exchange. These assumptions are (i) all three–particle irreducible graphs can be safely omitted and (ii) the two–quark correlations can be approximated by separable correlations, the so–called diquarks. The actual derivation of the Bethe–Salpeter equation for the effective baryon–diquark–quark vertex functions ϕ^a is presented in appendix A. Using the definitions for total and relative momentum given as in figure 2 this integral equation reads

4

$$\phi_{i,\alpha}^a(\bar{p}_i, P) = \sum_{bb'} \int \frac{d^4\bar{l}}{(2\pi)^4} \, K_{ij,\beta\alpha}^{ab}(\bar{p}_i, \bar{l}, P) \, G_{j,bb'}^{\beta\beta'}(\bar{l}, P) \, \phi_{j,\beta'}^{b'}(\bar{l}, P) \; + (j \longleftrightarrow k) \,. \tag{6}$$

Here G_j describes the disconnected quark–diquark propagator

$$G_{j,bb'}^{\beta\beta'}(\bar{l}, P) = S_j^{\beta\beta'}(\eta P + \bar{l}) \, D_{bb'}((1-\eta)P - \bar{l}) \; = \; S_j^{\beta\beta'}(l) D_{bb'}(P - l) \tag{7}$$

Furthermore, the quark–diquark interaction kernel K contains besides the propagator of the exchanged quark also the diquark amplitudes χ_i^a defined via the separability assumption

$$t_i(k_j, k_k; p_j, p_k) = \sum_{a,a'} \chi_i^a(k_j, k_k) \, D_{a,a'}(k_j + k_k) \, \bar{\chi}_i^{a'}(p_j, p_k) \tag{8}$$

of the quark–quark t–matrix (cf. App. A). The kernel explicitly reads

$$\begin{aligned} K_{ij,\beta\alpha}^{ab}(\bar{p}, \bar{l}, P) &= \bar{\chi}_{i,\beta\gamma}^a(\bar{l} + \eta P, q) \, S_k^{\gamma\gamma'}(q) \, \chi_{j,\gamma'\alpha}^b(q, \bar{p} + \eta P) \\ &= \bar{\chi}_{i,\beta\gamma}^a(l, q) \, S_k^{\gamma\gamma'}(q) \, \chi_{j,\gamma'\alpha}^b(q, p) \,, \end{aligned} \tag{9}$$

$$\text{with}$$

$$q = (1 - 2\eta)P - \bar{p} - \bar{l} \; = \; P - p - l \,,$$

since $P = p_i + p_j + p_k$ and $\bar{l} = l - \eta P$. The above relations also indicate the independence of the momentum partition parameter η since the Jacobian of the transformation $\bar{l} \to l$ equals unity for fixed total momentum P.

For the solution of the Bethe–Salpeter equation (6) we still have to choose the appropriate quantum numbers associated with baryons. This will be discussed in subsection B and we will find that the quark exchange (parameterized by the kernel K^{ab}) generates sufficient attraction to bind quarks and diquarks to baryons. For identical quarks antisymmetrization is required when projecting onto baryon quantum numbers. Fortunately, this does not alter the algebraic form of the Bethe–Salpeter equation (6). Rather, it simply implies that we may omit the single particle indices i on the quark propagators S_i. Only when caring about the discrete quantum numbers we have to revert to these indices since they specify the *summation order* over color, flavor and Dirac indices in eq. (6). Furthermore the functional forms of the diquark propagators $D_{aa'}$ and the vertices χ_i^a do not depend on the quark labels. These independencies are already indicated in eqs (7) and (9) as we have omitted the quark labels for the momenta.

In a self–consistent approach one would calculate the t–matrix from its own Bethe–Salpeter equation (A12). However, this is beyond the scope of the present investigation.
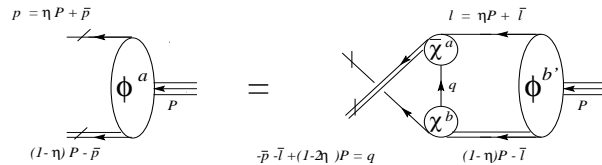

FIG. 2. The coupled set of Bethe-Salpeter equations for the effective vertex functions ϕ^a.

Instead we model the t–matrix by diquark correlators which have an analytic structure such that no particle interpretation for the diquark exists. We will restrict ourselves to the scalar and axialvector channels as these comprise the minimal set to describe octet and decuplet baryons. Furthermore these channels are generally assumed to be the most important ones, see refs. [1,2] and references therein. The corresponding separable *ansatz* for the two–quark t–matrix reads

$$ t_{\alpha\beta,\gamma\delta}(k_1, k_2; p_1, p_2) = \chi^5_{\alpha\beta}(\bar{k}, P_2) \, D(P_2) \, \bar{\chi}^5_{\gamma\delta}(\bar{p}, P_2) \; + \; \chi^\mu_{\alpha\beta}(\bar{k}, P_2) \, D^{\mu\nu}(P_2) \, \bar{\chi}^\nu_{\gamma\delta}(\bar{p}, P_2) \, . \quad (10) $$

Here we rewrite the diquark–quark vertices $\chi^{5[\mu]}$ as functions of relative, $\bar{k} = \sigma k_1 - (1-\sigma)k_2$, and total, $P_2 = k_1 + k_2 = p_1 + p_2$, momenta instead of the single quark momenta. In actual calculations, we choose for simplicity the symmetric momentum partition, *i.e.* $\sigma = 1/2$. Shifting the value of σ is possible, however, this complicates slightly the parameterization of diquark correlations, see the discussion below eq. (17) and in ref. [13].

The diquark propagators in the scalar and the axialvector channel are modeled as

$$ D(P) = -\frac{1}{P^2 + m_{sc}^2} \, f\left(\frac{P^2}{m_{sc}^2}\right) \, , \quad (11) $$

$$ D^{\mu\nu}(P) = -\frac{1}{P^2 + m_{ax}^2} \left(\delta^{\mu\nu} + (1 - \xi)\frac{P^\mu P^\nu}{m_{ax}^2} \right) f\left(\frac{P^2}{m_{ax}^2}\right) \, . \quad (12) $$

The dressing function $f(P^2/m^2)$ is hereby chosen identical to the one for the quark propagator, i.e. either one of the forms (3,4,5). Note that the choice $f(P^2/m^2) = 1$ and $\xi = 0$ corresponds to the free propagators of spin–0 and spin–1 particles. As a major purpose of the present paper we will study various deviations from the free propagators as an avenue to mimic confinement. In general, the dressing functions f are different in the scalar and axialvector channels as well as they are distinct from the one for the quark propagator. For simplicity, however, we will assume identical functions for all propagators. As we will not consider any axialvector diquark loops it is sufficient for the present purpose to use $\xi = 1$, see ref. [7] where it has been shown that choosing $\xi = 1$ leads to almost identical results for baryon amplitudes as $\xi = 0$.

If diquark poles existed in the t matrix, the diquark–quark vertices χ and χ^μ would on-shell ($P^2 = -m_{sc[ax]}^2$) correspond to diquark Bethe–Salpeter vertex functions. These vertex functions have a finite extension in momentum space and fall off fast enough to render all integrals finite. Empirically we assume that the corresponding scale is linked to the (inverse) proton radius. The conjugate vertex functions $\bar{\chi}$ are obtained by charge conjugation,

$$ \bar{\chi}^5(p, P) = C \, \left(\chi^5(-p, -P)\right)^T \, C^T \, , \quad (13) $$

$$ \bar{\chi}^\mu(p, P) = -C \, \left(\chi^\mu(-p, -P)\right)^T \, C^T \, , \quad (14) $$

where T denotes the transpose.

Let us now explicitly construct the vertex functions. They must be antisymmetric under the interchange of the two quarks. This entails

$$ \chi^{5[\mu]}_{\alpha\beta}(\bar{p}, P) = -\chi^{5[\mu]}_{\beta\alpha}(-\bar{p}, P)\Big|_{\sigma \leftrightarrow (1-\sigma)} \, . \quad (15) $$

6

Any two quarks within a baryon belong to the color antitriplet representation. Thus the diquark–quark vertices are proportional to the antisymmetric tensor ϵ_{ABD}. Here A and B are the color indices of the quarks whereas D labels the color of the diquark. Furthermore the scalar diquark is antisymmetric while the axialvector diquark is symmetric in flavor. We maintain only the dominant components with regard to the structure in Dirac space.[2] These are the antisymmetric matrix $(\gamma^5 C)$ for the scalar diquark and the symmetric matrices $(\gamma^\mu C)$ for the axialvector diquark. Considering, for the time being, only two flavors the vertices then read[3]

$$\chi^5_{\alpha\beta}(\bar{p}, P)|_{\sigma=1/2} = \chi^5_{\alpha\beta}(\bar{p}) = g_s(\gamma^5 C)_{\alpha\beta} \, V(\bar{p}^2) \, \frac{(\tau_2)_{ab}}{\sqrt{2}} \frac{\epsilon_{ABD}}{\sqrt{2}} \, , \tag{16}$$

$$\chi^\mu_{\alpha\beta}(\bar{p}, P)|_{\sigma=1/2} = \chi^\mu_{\alpha\beta}(\bar{p}) = g_a(\gamma^\mu C)_{\alpha\beta} \, V(\bar{p}^2) \, \frac{(\tau_2\tau_k)_{ab}}{\sqrt{2}} \frac{\epsilon_{ABD}}{\sqrt{2}} \, . \tag{17}$$

Choosing the scalar function V to depend only on the squared relative momentum $\bar{p}^2$, these vertices are indeed antisymmetric with respect to exchange of quark labels for the partition $\sigma = 1/2$. Otherwise a parametrization of V would depend on both $\bar{p}^2$ and $\bar{p} \cdot P$ in order to comply with antisymmetrization [13,48]. However, complete independence for observable quantities on σ could only be obtained by solving the Bethe–Salpeter equation (A12) for the two–quark t–matrix in which case the scalar functions V could depend on the quantity $(\bar{p} \cdot P)^2$ (for $\sigma = 1/2$) which is symmetric under quark exchange. In the actual calculations we will use a multipole form type *ansatz*

$$V(x) = V_n(x) = \left(\frac{\lambda_n^2}{\lambda_n^2 + x}\right)^n \, . \tag{18}$$

The overall strength of the diquark correlations given in eqs (16,17) is governed by the "diquark-quark coupling constants" g_s and g_a. They could be determined by either imposing the canonical Bethe–Salpeter norm condition on $\chi^{5[\mu]}$ or by the solution to the differential Ward identity for the diquark–photon vertex which is sensitive to the substructure of the diquarks [6]. For simplicity, we will fix g_s from fitting the nucleon mass. When including axialvector diquarks we will assume the ratio $g_a/g_s = 0.2$ as suggested by the results of ref. [6]. In this manner the baryon Bethe–Salpeter equation (6) becomes an eigenvalue problem for the coupling constants g_s and g_a.

Note that by parameterizing the quark–quark t–matrix we do not make any reference to the nature of the relevant quark–quark interaction. For example, to quantitatively include pionic effects we would have to solve Dyson–Schwinger equations for the quark propagator and the Bethe–Salpeter equation with explicit pion degrees of freedom. Studies within

---

[2]The complete Dirac structure for the scalar diquark containing four independent tensors can be obtained by analogy from the one for pseudoscalar mesons. The complete Dirac structure for the axialvector diquark consists of twelve independent terms, four longitudinal and eight transverse ones.

[3]In the compact notation the indices α and β of $\chi_{\alpha\beta}$ not only contain the Dirac labels but also those for flavor and color.

the Nambu–Jona–Lasinio model using diquark–quark correlations either in a soliton background [16] or with explicit pion interaction between the quarks [17] lead to a substantial gain in the binding energy. Since we determine the coupling constant g_s from the nucleon mass, those studies suggest that the inclusion of pion degrees of freedom would merely lead to a shift of this constant.

Equipped with the separable form of the two–quark correlations, see eq (10), and the functional form of the scalar and axialvector diquark correlations in eqs (16,17), we will set up the effective Bethe-Salpeter equation for the nucleon.

Upon attaching quark and diquark legs to the vertex functions ϕ one obtains the Bethe–Salpeter wave functions ψ. Equation (6) can then be rewritten as a system of equations for wave– and vertex functions as defined in Appendix B. Using the notations (B1–B3) we obtain

$$\int \frac{d^4k}{(2\pi)^4} G^{-1}(p,k,P) \begin{pmatrix} \Psi^5(k,P) \\ \Psi^{\mu'}(k,P) \end{pmatrix} = 0 . \tag{19}$$

Here $G^{-1}(p,k,P)$ is the inverse of the quark–diquark four–point function which results from the quark exchange[4]. It is the sum of the disconnected part and the interaction kernel which contains the quark exchange,

$$G^{-1}(p,k,P) = (2\pi)^4 \, \delta^4(p-k) \, S^{-1}(p_q) \, \circ D^{-1}(p_d) \tag{20}$$
$$-\frac{1}{2} \begin{pmatrix} -\chi^5(p_2^2) \, S^T(q) \, \bar{\chi}^5(p_1^2) & \sqrt{3} \, \chi^{\mu'}(p_2^2) \, S^T(q) \, \bar{\chi}^5(p_1^2) \\ \sqrt{3} \, \chi^5(p_2^2) \, S^T(q) \, \bar{\chi}^\mu(p_1^2) & \chi^{\mu'}(p_2^2) \, S^T(q) \, \bar{\chi}^\mu(p_1^2) \end{pmatrix} .$$

The flavor and color factors have been worked out and therefore $\chi^5(p^2)$ and $\chi^\mu(p^2)$ from now on only represent the Dirac structures of the diquark–quark vertices (multiplied by the invariant function $V_n(p^2)$, *cf.* eq (18)). The freedom to partition the total momentum between quark and diquark introduces the parameter $\eta \in [0,1]$ with $p_q = \eta P + p$ and $p_d = (1-\eta)P - p$. The momentum of the exchanged quark is then given by $q = -p - k + (1-2\eta)P$. The relative momenta of the quarks in the diquark vertices χ and $\bar{\chi}$ are $p_2 = p + k/2 - (1-3\eta)P/2$ and $p_1 = p/2 + k - (1-3\eta)P/2$, respectively. Invariance under (four dimensional) translations implies that for every solution $\Psi(p,P;\eta_1)$ of the Bethe–Salpeter equation a family of solutions exists that have the form $\Psi(p + (\eta_2 - \eta_1)P, P; \eta_2)$. Considering the Bethe–Salpeter equation as a linear eigenvalue problem for Ψ (or Φ) in the coupling constant g_s, translation invariance requires the coupling constant eigenvalue to be independent of η once a bound–state mass $-P^2 = M^2$ is fixed. This independence is exactly what one observes in the numerical solutions of the BSE, provided the analytic form of the dressing functions, eq (2)–(4), is used. However, the η–independence is lost when substituting non–analytic propagators such as those parameterized by the function f_3, eq (5). Essentially the reason is that Cauchy's theorem does not apply to non–analytic functions. The difference in the eigenvalues of the Bethe–Salpeter equation under the variation of η can be shown to equal a contour integral in the complex p–plane. This integral vanishes only if the integrand is an analytic function. However, when choosing $d > 5$ in eq (5),

---

[4]For convenience we have omitted the discrete labels.

the propagator resembles the free propagator in a large domain thereby mitigating the η–dependence.

The structure of the equations for the octet baryons is similar to that of the nucleon (19). However, the number of Dirac structures Φ^5 and Φ^μ increases due to the possible different quark–diquark flavor configurations. These equations are given in full detail in refs. [7,18]. Allowing for flavor symmetry breaking, that is induced by a difference between the masses of strange quark and up/down quark, discriminates vertex functions Φ^5 and Φ^μ with different diquark configurations [7]. As the Λ hyperon presently is of special interest, we list its three different correlations,

$$\Phi_\Lambda \sim \Phi^5_{F_1}, \quad \Phi^5_{F_2} \quad \text{and} \quad \Phi^\mu_L . \tag{21}$$

Here, $F_1 = \{d[us] - u[ds]\}/\sqrt{2}$, $F_2 = s[ud]$ and $L = [d\{us\} - u\{ds\}]/\sqrt{2}$ refer to different quark–diquark flavor states. Antisymmetrized scalar diquarks are denoted by square brackets $[\ldots]$ and symmetrized axialvector diquarks by curly brackets $\{\ldots\}$. Note that broken $SU(3)$–flavor symmetry induces a component of the total antisymmetric flavor singlet $\frac{1}{\sqrt{3}}[[su]d + [ud]s + [ds]u]$ into wave and vertex functions. In non–relativistic quark models with $SU(6)$ symmetry such a component is forbidden by the Pauli principle, however, having non–vanishing lower components in the baryon bi–spinors does actually lead to such flavor singlet components. In actual calculations they turn out to be small [7].

B. Electromagnetic form factors

To further constrain the model parameters, we calculate the electromagnetic form factors of the nucleon. In this section we provide the formalism and the corresponding results will be given in subsection V A. These form factors parameterize the nucleon matrix element of the current operator that describes the coupling of the photon to quark and diquark within the nucleon. Gauge invariance and the proper normalization of the nucleon charges are ensured when the current operator comprises all possible couplings to the inverse quark–diquark four–point function G^{-1} of eq (19) [13,6,18]. The current operator is sandwiched between the Bethe–Salpeter wave–functions $\bar{\Psi}$ and Ψ of the final and initial state, respectively, according to Mandelstam's recipe [19]. In total, we have contributions from the *impulse approximation* which are described by the upper diagrams in figure 3 and contributions from the *Bethe–Salpeter kernel* which are given by diagrams of the type given in the lower part of figure 3.

To calculate the form factor diagrams, we need properly normalized Bethe–Salpeter wave–functions. This normalization is obtained from

$$M_N \Lambda^+ \overset{!}{=} - \int \frac{d^4 p}{(2\pi)^4} \int \frac{d^4 k}{(2\pi)^4} \bar{\Psi}(k, P_n) \left[P^\mu \frac{\partial}{\partial P^\mu} G^{-1}(k, p, P) \right]_{P=P_n} \Psi(p, P_n) , \tag{22}$$

where M_N is the nucleonic bound state mass. The conjugated wave–function $\bar{\Psi}$ is in analogy with eqs (13) and (14) given by

$$\bar{\Psi}(k, P_n) = \eta_d \, C \, \Psi(-k, -P_n)^T \, C^T \tag{23}$$

with $\eta_d = 1$ and $\eta_d = -1$ when the involved diquark is respectively of scalar or axialvector type.
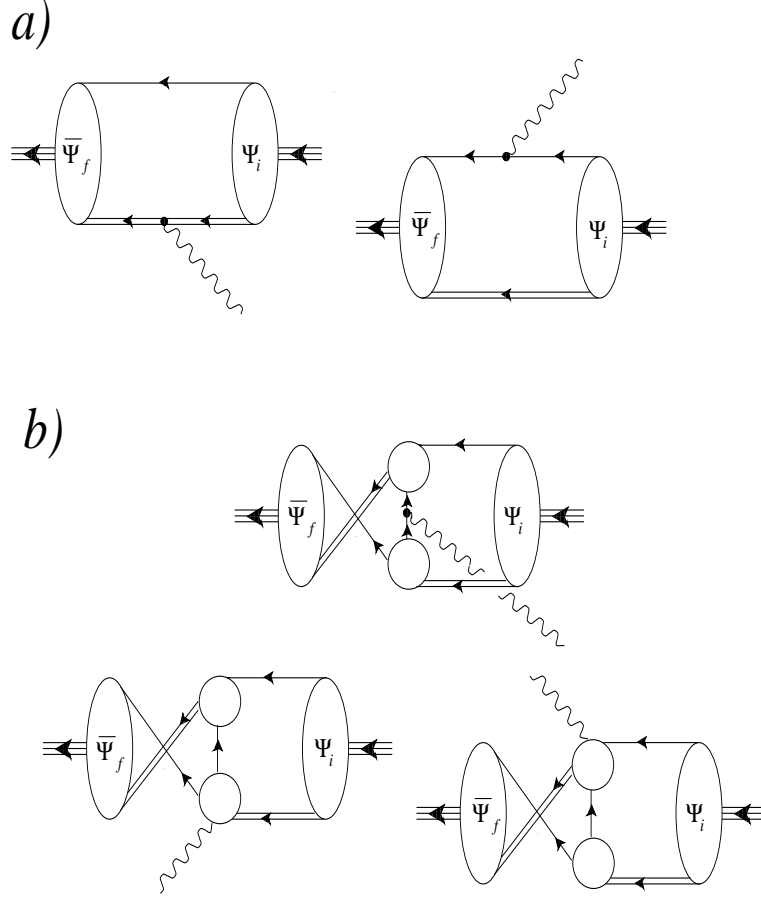
FIG. 3. Contributions from the impulse approximation (a) and from the Bethe–Salpeter kernel (b) to the electromagnetic form factors.

Furthermore we need expressions for the photon vertices that appear in the diagrams. In ref. [13] the seagull vertices describing the photon coupling to the diquark–quark vertices χ have been derived for the scalar diquark. The coupling of the axialvector diquark to the photon has been studied in ref. [6]. The photon vertices with quark and diquark must fulfill the differential Ward identities for zero momentum transfer to the photon

$$\Gamma_q^\mu(p_q, p_q) = \frac{\partial}{\partial p_q^\mu}\, S^{-1}(p_q)\,,\tag{24}$$

$$\tilde{\Gamma}_d^\mu(p_d, p_d) = \begin{pmatrix} \Gamma_s^\mu & 0 \\ 0 & \Gamma_a^\mu \end{pmatrix} = \frac{\partial}{\partial p_d^\mu}\, \tilde{D}^{-1}(p_d)\,.\tag{25}$$

Here $\tilde{\Gamma}_d^\mu$ comprises both photon vertices with scalar and axialvector diquarks. For convenience the discrete labels have been omitted. The Ball–Chiu construction of the longitudinal part of the vertices ensures that they obey both the differential Ward as well as the Ward–Takahashi identity. The latter identities constrain the vertices for finite Q. For the dressed quark propagators of eq (1) the corresponding vertices finally read

10

$$\Gamma_{q,i}^{\mu}(k_q, p_q) = -\frac{i}{2}\,\gamma^{\mu}\left[1/f_i(k_q^2/m_q) + 1/f_i(p_q^2/m_q)\right]$$
$$-\frac{i}{2}\,(k_q + p_q)^{\mu}\,\frac{1/f_i(k_q^2/m_q) - 1/f_i(p_q^2/m_q)}{k_q^2 - p_q^2}\,[(\slashed{k}_q + \slashed{p}_q) - 2im_q]\;. \qquad (26)$$

This construction is valid for the analytic dressing functions f_0, f_1 and f_2.

In the case of the non–analytic dressing function f_3, we must specify the derivatives in eqs (22–25) with respect to the total bound state momentum P and the quark and diquark momenta p_q and p_d, respectively. We calculate form factors in the Breit frame, *i.e.* the temporal component of the momentum transfer is zero. Consequently, the relative momenta between the initial quark, k and the final diquark, p are real. They must be integrated over in the norm integral (22) and in the calculation of the diagrams of figure 3. Let us consider the quark momenta which are defined as before: $k_q = \eta P_f + k$ and $p_q = \eta P_i + p$. We define the derivatives in equations (22), (24) and (25) as follows,

$$\frac{\partial}{\partial P_{i[f]}} = \eta\frac{\partial}{\partial p[k]}\;, \qquad \frac{\partial}{\partial p_q[k_q]} = \frac{\partial}{\partial p[k]}\;. \qquad (27)$$

Of course, these are trivial identities when applied onto analytical functions. Derivatives with respect to the diquark momenta are defined accordingly. The nucleon charges obtained as the form factors at zero momentum transfer are then properly normalized. The corresponding proof utilizes the methods outlined in ref. [13].

To comply with the Ward–Takahashi identity, the quark–photon vertex has to be modified

$$\Gamma_{q,3}^{\mu} = -\frac{i}{2}\,\gamma^{\mu}\left(1/f_3(k_q^2/m_q^2, k_q^{*2}/m_q^2) + 1/f_3(p_q^2/m_q^2, p_q^{*2}/m_q^2)\right)$$
$$-\frac{i}{2}\,(k_q + p_q)^{\mu}\,\frac{1/f_3(k_q^2/m_q^2, p_q^{*2}/m_q^2) - 1/f_3(p_q^2/m_q^2, p_q^{*2}/m_q^2)}{k_q^2 - p_q^2}\,[(\slashed{k}_q + \slashed{p}_q) - 2im_q]$$
$$-\frac{i}{2}\,(k_q^* + p_q^*)^{\mu}\,\frac{1/f_3(k_q^2/m_q^2, k_q^{*2}/m_q^2) - 1/f_3(k_q^2/m_q^2, p_q^{*2}/m_q^2)}{k_q \cdot k_q^* - p_q \cdot p_q^*}\,[(\slashed{k}_q + \slashed{p}_q) - 2im_q]\;. \qquad (28)$$

This vertex now depends on the four variables k_q, k_q^*, p_q and p_q^* and is also non–analytic as is the corresponding quark propagator $S^{(3)}$. The photon Ball–Chiu vertices with scalar and axialvector diquarks have to be modified using an analogous description [18]. The coupling of the photon to the anomalous magnetic moment of the axialvector diquark and the vertex for photon–induced anomalous scalar–axialvector diquark transitions are transversal and need not be modified [6].

C. Strong Form Factors

Here we consider the strong form factors $g_{\pi NN}$ and $g_{KN\Lambda}$. These quantities are not only interesting in themselves but also enter the calculation of production processes like $p\gamma \to \Lambda K$ or associated strangeness production $pp \to pK\Lambda$.

In figure 4 we show the dominant contributions to the strong form factors. Here the meson directly couples to one of the baryon constituents. Keeping only such direct couplings while
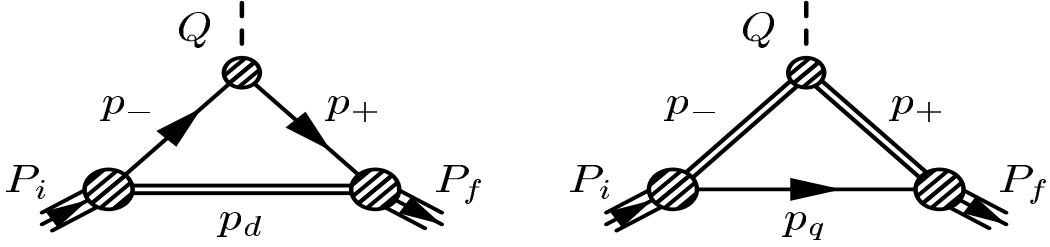
FIG. 4. Dominant diagrams for the strong form factors $g_{\pi NN}$ and $g_{KN\Lambda}$. The incoming proton carries the momentum P_i while P_f is associated with the outgoing baryon. The incoming meson carries the momentum Q and couples to the quark (*left panel*) or to the diquark (*right panel*).

omitting those to the exchanged quark defines the impulse approximation that we will adopt here[5]. The two diagrams shown in figure 4 actually correspond to a number of diagrams which differ by the type of the involved diquarks. Let us first consider the process in which the meson couples to the quark. For $g_{KN\Lambda}$ only one possibility exists: the diquark has to be a scalar ud–diquark since this is the only overlap between the wave–function of the proton and the wave–function of the Λ. For $g_{\pi NN}$ both scalar and axialvector diquarks need to be taken into account. The second important contribution represents the coupling of the meson to the diquark. For the diquark part we do not have to distinguish between $g_{\pi NN}$ and $g_{KN\Lambda}$. That is, in both cases the diquark associated with the momenta p_+ or p_- may be scalar or axialvector.

The meson–quark vertex is the solution of a separate Bethe–Salpeter equation which has been extensively studied, see [2] and references therein. In the chiral limit this Bethe–Salpeter equation becomes formally identical to the Dyson–Schwinger equation for the scalar self energy function $B(p^2)$ when only the leading Dirac structure is considered, *i.e.*

$$\text{(diagram)} \quad = \Gamma_m(p_-, p_+) = \frac{i}{2f}\gamma_5\left\{B(p_+^2) + B(p_-^2)\right\}. \tag{29}$$

Here f is the meson decay constant.

The structure of the meson–diquark vertices is constrained not only by Lorentz covariance and parity but also by the Bose–statistics for the two involved diquarks. We thus parameterize the pseudoscalar meson axialvector diquark vertex as

$$\Gamma_{aa}^{\rho\lambda} = -i\frac{\kappa_{aa}}{2M}\frac{m}{f}\epsilon^{\rho\lambda\mu\nu}(p_- + p_+)^\mu Q^\nu. \tag{30}$$

Here the superscripts ρ, λ denote the Lorentz indices of the incoming and outgoing axialvector diquark, respectively. The nucleon mass M has been introduced to define the

---

[5]Contributions to the nucleon electromagnetic form factors beyond the impulse approximation that arise from the coupling to the exchanged quark have been thoroughly discussed in refs [6,13,18].

dimensionless coupling constant κ_{aa}. Furthermore m is the average of the masses of the constituent quarks in the diquarks. The corresponding *ansatz* for the scalar–axialvector transition reads,

$$\Gamma_{sa}^{\rho} = -\kappa_{sa}\frac{m}{f}Q^{\rho}\,, \tag{31}$$

where the definitions are those of eq (30) and κ_{sa} is again a dimensionless constant specifying the overall strength of the vertex. The vertex (31) describes the coupling of the diquarks to the derivative of the pseudoscalar mesons. Such a construction is suggested by the chiral structure of the strong interactions that can be written as expansion in the derivatives of the Goldstone bosons, at least in the chiral limit.

Having collected all ingredients we may now proceed and compute the diagrams in figure 4. According to the Mandelstam formalism [19] the diagram shown in the left panel translates into an expression of the form

$$\int \frac{d^4q}{(2\pi)^4}\,\bar{\Phi}_f(q_f, P_f)S(p_+)\Gamma_m(p_-, p_+)S(p_-)\Phi_P(q, P_i)D(p_d)\,, \tag{32}$$

where we only indicated the general structure, *i.e.* we omit indices that are associated to the coupling and propagation of axialvector diquarks. The conjugated vertex function, $\bar{\Phi}$ relates to the vertex function, Φ as the conjugated wave function (23) to the wave function:

$$\bar{\Phi}(p, P) = \eta_d\, C\, \Phi(-p, -P)^T\, C^T \tag{33}$$

with $\eta_d = 1$ and $\eta_d = -1$ when the involved diquark is respectively of scalar or axialvector type. We note that $\bar{\Phi}(p, P)$ also solves the Bethe–Salpeter equation (6). We denote the loop momentum by q and introduce the momentum partition,

$$p_- = q + \eta P_i\,, \quad p_+ = p_- + Q = q_f + \eta P_f \quad \text{and} \quad p_d = -q + (1 - \eta)P_i\,. \tag{34}$$

Again, $\eta \in [0, 1]$ is the momentum partition parameter. For the diagram in the right panel quark and diquark propagators need to be exchanged.

III. BOUND STATE REACTIONS AND KINEMATICAL CONDITIONS FOR COMPLEX MOMENTA

In this section we will discuss that regime in the complex momentum plane where we need to know the quark and diquark propagators in order to solve the Bethe–Salpeter equation (19) and compare that regime to the one that enters the computation of the production processes like $p\gamma \to \Lambda K$ and $pp \to pK\Lambda$. In principle these propagators can be calculated using Dyson–Schwinger equations [2] and also respective lattice measurements should be available in the near future; for preliminary results see *e.g.* refs. [20,21]. Both methods comprise the non–perturbative dynamics and should therefore give the basic ingredients to describe hadrons as bound state of quarks. However, both approaches are set up in Euclidean space and one has to revert to extrapolations when the propagators are demanded for timelike momenta. If we wanted to perform an appropriate analytic continuation from
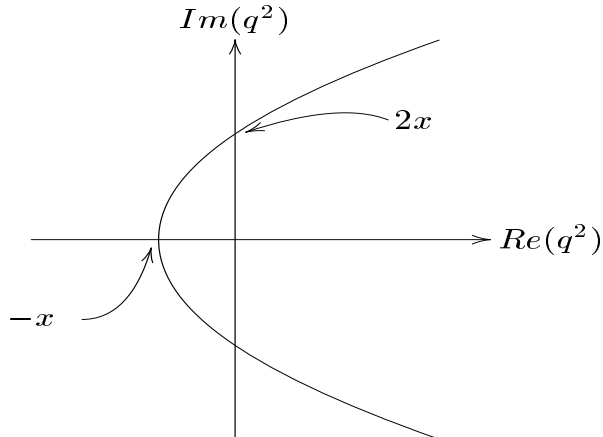
FIG. 5. The complex q^2–plane. The interior of the parabola is needed for the calculation of the diagram in the left panel of figure 6, x is defined as $x = (\eta M + E)^2$. Note that in the case of the Bethe–Salpeter equation we substitute $x = \eta^2 M^2$.

Euclidean back to Minkowski space we would even require the propagators in a region of the complex momentum plane[6]. In order to calculate amplitudes of physical processes between on–shell particles using the Euclidean Bethe–Salpeter formalism the temporal components of the external momenta must be purely imaginary. In this framework the momenta become complex. In these calculations therefore the structure of the propagators in the complex momentum plane is essential. Furthermore, it is important for the phenomenological parameterization of confinement. As repeatedly mentioned we comprehend the confinement phenomenon as the absence of poles on the timelike q^2–axis in the propagator of colored "particles".

The Bethe–Salpeter equation is most conveniently solved in the rest frame of the bound state, $P = (\vec{0}, iM)$. Here we want to specifically discuss the kinematical domain that is probed by the (di)quark propagators in the bound state rest frame. In eq (19) the loop momentum, k, relative between quark and diquark is chosen to be real. Hence the temporal component of the quark momentum $k_q = \eta P + k$ becomes complex. The values of k_q^2 that are covered when integrating over k lie within a parabola that opens towards the spacelike axis, *cf.* figure 5. The intercept of the parabola with the real axis is at (small) timelike $k_q^2 = -(\eta M)^2$. Thus, solving the Bethe–Salpeter equation mainly probes the behavior of the quark propagator for spacelike momenta. Since mainly the spacelike momenta are relevant, the propagators that are parameterized by the dressing function (4) approach the free propagators in the limit $d \rightarrow +\infty$. In this limit the dressing functions (3) and (5) approach the bare propagators, both in the spacelike and timelike regions.

Next we will explore the q^2 regime relevant for production processes like kaon photopro-

---

[6]In the Dyson–Schwinger approach the corresponding integral equation should be used for this analytic continuation. Relying on a numerical solution that is only known for a finite set of Euclidean momenta is not sufficient because its analytic continuation away from that set cannot be determined.
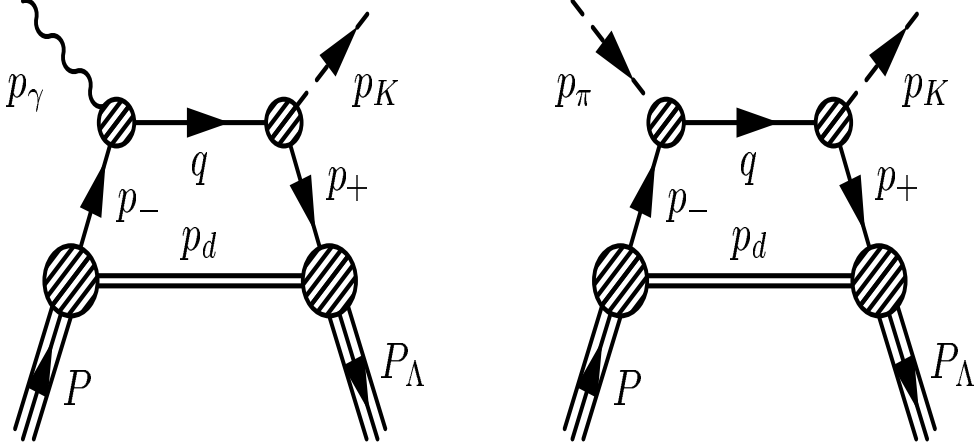
FIG. 6. *Left panel:* Main contribution to kaon photoproduction $p\gamma \to K\Lambda$, *right panel:* Handbag diagram contributing to the reaction $pp \to pK\Lambda$ as a subprocess. The incoming pion couples to the 'spectating' proton.

duction. The contribution to the reaction $p\gamma \to \Lambda K$ that involves a quark loop is shown in the left panel of figure 6. It turns out that it suffices to consider a parabola shaped region of the complex q^2–plane (*i.e.* it is sufficient to consider only this momentum and ignore the others). This can be understood in at least two ways: We could use the wave–functions rather than the vertex–functions for the calculation of the diagram. In this case the propagators that depend on p_q, k_q and p_d are included in the wave–functions and there would be no necessity to treat them separately. Nevertheless, considering the propagators $S(p_q), S(q), S(k_q)$ and $D(p_d)$ separately we find that among all the internal momenta in the diagram it is q that reaches farthest in the timelike regime. Thus the following analysis for p_q and k_q would yield less restrictive conditions.

From the momentum routing shown in the left panel of figure 6 we have:

$$q = p_- + p_\gamma = \eta P + l + p_\gamma \tag{35}$$

where η is the momentum partition parameter ($p_- = \eta P + l$, $p_d = (1 - \eta)P - l$) while l refers to the loop momentum. We chose the loop momentum to be real which implies that the external momenta like P and p_γ must have an imaginary temporal component in order to correspond to physical particles. For the following kinematical considerations we choose the proton rest frame and take the photon to propagate along the y-axis,

$$P = (\vec{0}, iM), \quad p_\gamma = (0, E, 0, iE), \quad l = (\vec{l}, l_4) \tag{36}$$

Hence the momentum entering the quark propagator becomes

$$q^2 = \left(-\eta^2 M^2 + l^2 - 2\eta ME + 2El_y\right) + i\left(2\eta M + 2E\right)l_4, \tag{37}$$

where the real and imaginary parts of q^2 have been separated. This shows that we need to know the propagator $S(q^2)$ at complex q^2 in order to be able to compute the handbag diagram shown in the left panel of figure 6. The set of values of q^2 that occur has already been shown in figure 5. The situation seems to be completely parallel to what we found for

15

the Bethe–Salpeter equation; in both cases we need to know the propagators in a parabola shaped region of the complex plane. The intercept with the imaginary axis is in both cases minus two times the intercept with the real axis. However, there is one important difference. For the production processes the intercept with the real axis does depend on the photon energy E, more precisely: $-x = -(\eta M + E)^2$. Thus for $E = 0$ the computation of the handbag diagram shown in figure 6 uses the same region of the complex plane that is necessary to solve the Bethe–Salpeter equation. However, for $E > 0$ the parabola is shifted in the direction of the negative real axis.

The threshold for kaon photoproduction is at E slightly less than 1GeV and the cross section has been measured [22] up to $E \approx 2$GeV. This implies that the handbag diagram 'probes' the quark propagator *much* farther into the timelike region than the Bethe–Salpeter equation.

The second production process we are especially interested in is associated strangeness production, $pp \to pK\Lambda$. This reaction can be described similarly to the standard picture of the nucleon–nucleon interaction by one–boson exchange. That is, one of the incoming protons acts as a meson source and the emitted off–shell meson couples to one of the constituents of the baryon; the corresponding subprocess is shown diagrammatically in figure 6.

The analogous kinematical analysis for strangeness–production exhibits the same qualitative features. That process as well 'probes' a parabola shaped subset of the complex plane, whereby the parabola is somewhat broader than the one in figure 5. However, there again is an important difference: the parabola does extend only up to $q^2 \approx -0.53$GeV^2 into the timelike region. That is, the reaction $pp \to pK\Lambda$ 'probes' the propagators in essentially the same region as the Bethe–Salpeter equation does. It is therefore not as sensitive as kaon photoproduction to the behavior of the propagator in the timelike region.

The main conclusion of the above discussion is that certain production processes may be significantly more sensitive to the structure of the (di)quark propagators than the Bethe–Salpeter equation and thus the baryon spectrum. Hence the study of such processes should provide important information about these propagators.

IV. PRODUCTION PROCESSES IN THE DIQUARK–QUARK MODEL

In this section we present the key issues of the formalism to compute the cross sections for kaon photoproduction, $\gamma p \to \Lambda K$ and the associated strangeness production, $pp \to pK\Lambda$. In the diquark–quark model relatively few diagrams contribute to these processes and therefore we may analyze these reactions in detail. For further details on the definition of the involved observables and the relevant kinematics we refer the reader to appendix C.

As already indicated in the discussion of the strong form factors we consider the pseudoscalar mesons as additional model degrees of freedom. This does not imply any double counting because the model interaction (diquark exchange) does not lead to bound (would–be) Goldstone bosons. Thus we also include intermediate pseudoscalar mesons at tree level when computing the above mentioned observables. The relevant diagrams are shown in figures 7 and 8. As a general remark we note that these diagrams need to be computed in any covariant diquark–quark model. However, the propagators that are essential components of these diagrams are specific to our model, *cf.* eqs (2)–(5). Furthermore, the covariant wave– or vertex–functions that also enter these diagrams are obtained as solutions of the
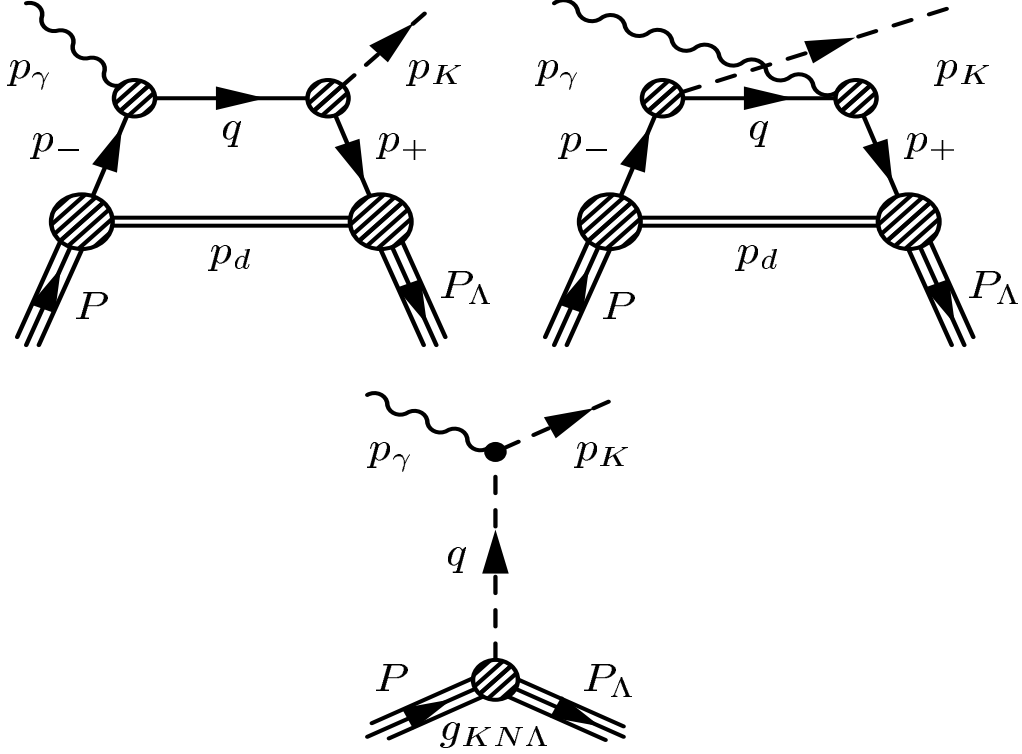
FIG. 7. Main contributions to kaon photoproduction $p\gamma \to \Lambda K$. The incoming proton and the outgoing Λ carry the momenta P and P_Λ respectively. The lower part of the figure shows the tree level diagram that models the exchange of a virtual kaon.

Bethe–Salpeter equation. Since this equation is subject to the model propagators they enter the calculation not only explicitly but also implicitly.

A. Kaon Photoproduction

In this subsection we will discuss kaon photoproduction $p\gamma \to \Lambda K$ within our covariant diquark–quark model. Some more details and technicalities of the calculation are given in appendix C 1.

We show the dominant diagrams in figure 7. The internal momenta of the (uncrossed) 'handbag diagram' are defined according to

$$p_- = p + \eta_p P, \quad p_d = -p + (1 - \eta_p)P, \quad q = p_- + p_\gamma,$$
$$p_+ = q - p_K, \quad P_\Lambda = P + p_\gamma - p_K, \quad p_f = p + (1 - \eta_p)P - (1 - \eta_\Lambda)P_\Lambda. \tag{38}$$

Here η_p and η_Λ are the momentum partition parameters of the proton and the Λ, respectively. Both, η_p and η_Λ can be chosen independently in the range $0 \leq \eta_p, \eta_\Lambda \leq 1$.

The two 'handbag diagrams' model the coupling to one of the constituents. They are calculated within the Mandelstam formalism. This yields

diagram #	1	2	3,5	4
diquark content	s	s,a	asa, aas, aaa, sas, saa	sas, saa

TABLE I. The diquark content of the diagrams shown in figure 8 with the numbers referring to the specific diagram. Here 's' and 'a' indicate scalar and axialvector diquark respectively. A sequence with three entries runs clockwise and starts at the incoming proton.

$$A_1 = i \int \frac{d^4p}{(2\pi)^4} \left\{ \bar{\Phi}_\Lambda(p_f, P_\Lambda) S(p_+) \Gamma_K(q, p_+) S(q) \right\} \left\{ \Gamma_\gamma(p_-, q) S(p_-) \Phi_P(p, P) D(p_d) \right\} \quad (39)$$

for the amplitude of the uncrossed handbag diagram. Here $\bar{\Phi}_\Lambda$ and Φ_p are respectively the vertex–functions of the Λ and the proton as discussed in section II. Furthermore Γ_K is the meson–quark vertex that has been discussed in the preceding subsection. The photon–quark coupling, Γ_γ is described by the Ball–Chiu vertex [23] or its generalization to the case of non–analytic propagators, see section II. The Ball–Chiu vertex has been constructed to satisfy the Ward identity. It reduces to the bare vertex in the limit that both momenta p and q are large. The Ward identity constrains only the longitudinal part of the vertex. Various *ansätze* for the transversal part of the vertex have been proposed (*cf.* ref [2] and references therein). While those *ansätze* solve problems related to multiplicative renormalizability and gauge invariance, the transversal part is generally assumed to be of minor influence on the resulting cross sections. Thus we will henceforth neglect the transversal part of the quark–photon vertex. Although the form of this vertex is not model specific, it contains the self–energy functions and thus it implicitly depends on the model propagators. The expression for the crossed handbag diagram can be easily inferred. The tree level diagram models the exchange of a virtual kaon and is expected to yield a non–negligible contribution for large photon energies. For the photon–meson coupling we use a bare vertex multiplied with the kaon electromagnetic form factor (see Appendix C 1) while the meson–baryon vertex is proportional to $g_{KN\Lambda}(Q^2)$ that has been discussed in subsection II C.

The 'handbag diagrams' shown in figure 7 probe the propagators not only for space-like momenta but also for comparably large timelike momenta, as we have emphasized in section III. This sensitivity to the behavior of the propagators for timelike momenta distinguishes the reaction $p\gamma \rightarrow \Lambda K$ from most other production processes.

B. Associated Strangeness Production

Here we apply the covariant diquark–quark model to associated strangeness production, $pp \rightarrow pK\Lambda$. Again, some technicalities are relegated to appendix C 2. We describe the reaction $pp \rightarrow pK\Lambda$ as a sum over one–boson exchange contributions for which we consider the exchange of pions and kaons. The main contributions are shown in figure 8. Other diagrams like planar kaon exchange or crossed pion exchange with couplings to the quark are excluded by the flavor algebra. We neglect diagrams in which the exchanged particle and the emitted kaon couple to different constituents, because they imply a large relative momentum at the baryon vertex which is strongly suppressed. In addition we omit the direct coupling of the pion to the emitted kaon.
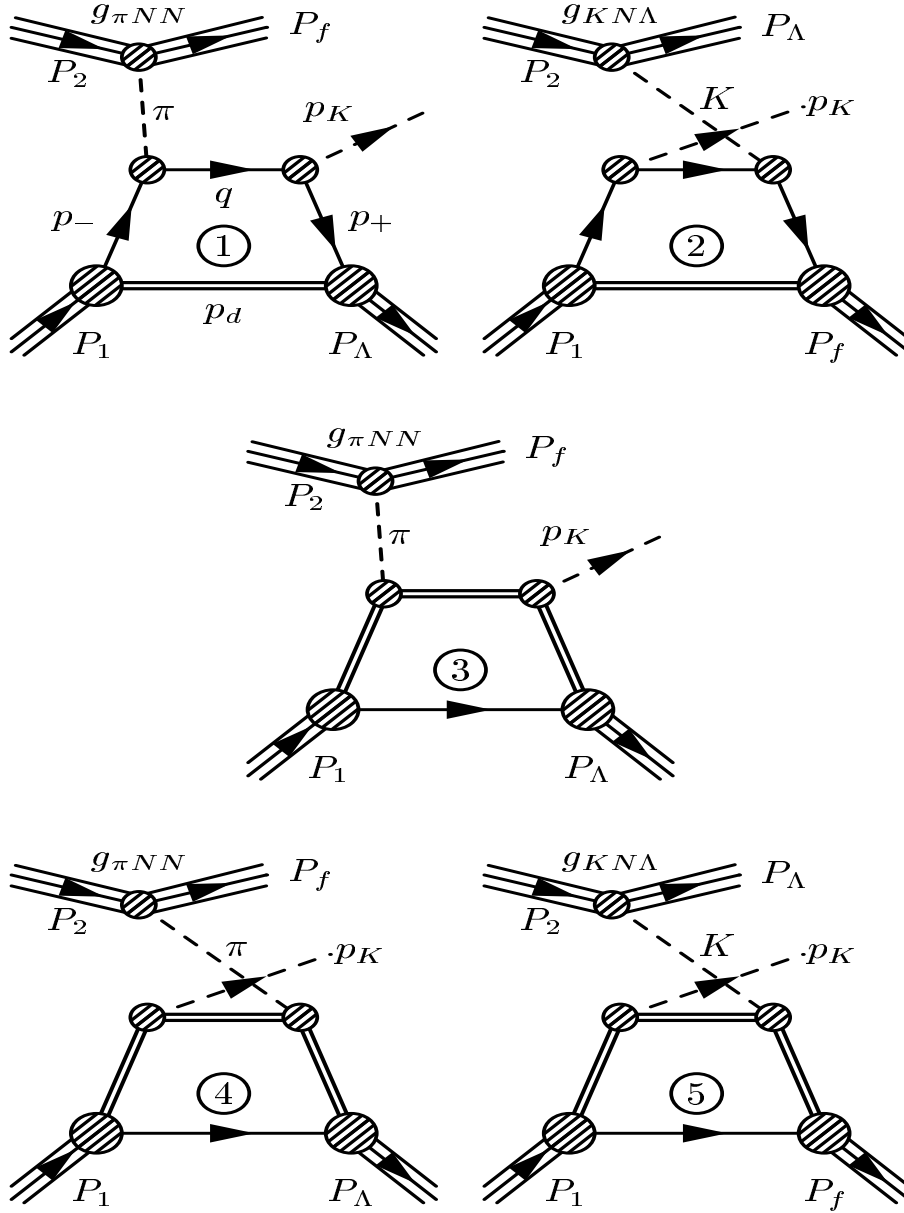
18

FIG. 8. Main contributions to associated strangeness production $pp \to pK\Lambda$. The momenta of the initial protons are given by P_i, $i = 1, 2$. The momenta of the final proton and Λ are denoted by P_f and P_Λ, respectively. p_K refers to the momentum of the final kaon. The diquark content of the diagrams is listed in Table I.

Similar to the calculation of $g_{KN\Lambda}$ in section II C, the flavor content of the Λ prohibits an axialvector diquark in the pion exchange diagram #1. However, this does not apply to the kaon exchange diagram #2 as the diquark mediates between two protons. Due to parity conservation we only have to consider scalar–axialvector and axialvector–axialvector diquark transitions at any meson–diquark vertex. Flavor algebra also shows that the axialvector diquark components of the incoming proton cannot contribute in diagram #4. The diquark content of the diagrams shown in figure 8 is listed in table I. Counting the diquark combinations in table I we arrive at 15 diagrams. This number is actually doubled because all diagrams have to be antisymmetrized with respect to the two incoming protons.

As an example, we outline the calculation of one of the two planar pion exchange diagrams. The calculation of the other diagrams is very similar. The amplitude of diagram #1 can be factorized according to

$$\mathcal{M} = \mathcal{L}\left(\frac{i}{Q^2 + m_\pi^2}\right)\mathcal{H}, \tag{40}$$

where $\mathcal{L}$ denotes the form factor part and $\mathcal{H}$ denotes the loop part of the diagram. The mass and the momentum of the intermediate pion are denoted by m_π and Q, respectively. The factor $\mathcal{L}$ essentially equals $g_{\pi NN}$,

$$\mathcal{L}_{s,s'} = \bar{u}_{s'}(P_f)\, i\gamma_5\, g_{\pi NN}(Q^2)\, u_s(P_2), \tag{41}$$

with spinor indices s and s'. In the remaining 'handbag part' $\mathcal{H}$ the conventions for the loop momenta can be extracted from diagram #1 of figure 8. Essentially they are given in eq (38) with the substitution $p_\gamma \to Q$ and similarly for the baryons. The 'handbag part' of the pion exchange diagram can then be written as

$$\mathcal{H} = i\int \frac{d^4p}{(2\pi)^4}\left\{\bar{\Phi}_\Lambda(p_f, P_\Lambda)\, S(p_+)\, \Gamma_K(p_+, q)\, S(q)\right\}\left\{\Gamma_\pi(q, p_-)\, S(p_-)D(p_d)\, \Phi_P(p_1, P_1)\right\}, \tag{42}$$

where isospin as well as Lorentz indices have been omitted for simplicity.

V. NUMERICAL RESULTS

After having outlined the model calculation we are now prepared to present the numerical results. Here we focus on studying the effects of the different model propagators (2)–(5) on the calculation of and the predictions for the above mentioned processes.[7] As mentioned earlier, this is the main purpose of the present study. Numerical results for the form factors obtained with the tree level propagators (2) can be found in ref. [6].

------

[7]A few selected numerical results using other forms of dressed model propagators have been published in refs. [24].

A. Parameter Fixing: Masses and Electromagnetic Form Factors

We fix the model parameters, see table II, from the octet baryon masses and the nucleon magnetic moments. The numerical details for solving the octet baryon Bethe–Salpeter equations and the computation of the form factors are thoroughly discussed in ref. [18].

Within the required numerical accuracy we have assured the above described independence of the octet masses of the momentum partition parameter η when analytical propagators are used. As argued before, this invariance does not hold for non–analytic propagators. In these cases we chose η to be close to its non–relativistic value $m_q/(m_q + m_d)$ where m_q and m_d denote quark and diquark mass parameters of the flavor channel associated with the considered baryon. This choice is natural since other ones yield larger eigenvalues of the Bethe–Salpeter equation. We take the physical nucleon mass to fix the scalar diquark coupling g_s and the Λ mass to determine the strange quark mass parameter m_s. By reproducing the phenomenological dipole fit for the proton electric form factor, G_E we essentially fix the diquark width λ. Subsequently we are enabled to compute the proton and neutron magnetic moments, μ_p and μ_n as well as the masses of the Σ and Ξ baryons. For that calculation we assume isospin symmetry, $m_u = m_d$.

In table II we list the six parameter sets that we will employ to compute the strong form factors and observables of production processes later on. The first four sets are restricted to the dominant scalar diquark correlations. In set I we consider the pole–free exponential dressing function, f_2, while the sets II and III are associated with dressing functions of the Stingl type, f_1. These two sets differ by the value of d that characterizes the separation of the complex conjugated poles. Finally set IV assumes the non–analytic pole–free dressing function, f_3. As already indicated the dressing of the propagators increase the predicted proton magnetic moment when all other model parameters remain unchanged. Using the parameters of set II but free propagators yields $\mu_p = 2.27$ while the Stingl–type propagators result in $\mu_p = 2.46$ and $\mu_p = 2.64$ for $d = 8.0$ and $d = 4.0$, respectively. The magnetic moment of the proton falls a little short for the sets II and IV. The overall picture emerges that the restriction to only scalar diquark correlations produces too large ratios $|\mu_n/\mu_p|$ and rather large mass splittings between the octet baryons, especially between Σ and Λ.

As shown in figure 9 all sets reasonably well reproduce the electric form factor, G_E. Our results are confined within a region that is characterized by less than approximately 15% deviation from the dipole fit. This deviation, although rectifiable by refining the time–consuming parameter search, is of no significance for the conclusions that we will draw from our results for the production processes. This will become clear from the discussions in section V D.

The calculations with the parameters sets V and VI include a moderate admixture of axialvector diquarks, $g_a/g_s = 0.2$. For simplicity the axialvector diquark masses are chosen identical to the scalar ones. Here we particularly consider the Stingl form, f_1 (set V) and the non-analytic form, f_3 (set VI) since later we will find that the exponential form, f_2 produces unacceptable results for the production processes. Upon inclusion of the axialvector diquark the good description of G_E remains unchanged while the ratio $|\mu_n/\mu_p|$ and the mass splitting between Σ and Λ even improve. For set VI the predicted octet masses are almost indistinguishable from their experimental values. As already observed in ref. [6] and as is exhibited in the right panel of figure 9, the ratio G_E/G_M calculated with axialvector diquarks

diquark:	I	II	III	IV	V	VI	expt.
		only scalar			scalar and axialvector		
f_i	2	1	1	3	1	3	
d	2.0	8.0	4.0	6.0	4.0	6.0	
$m_u = m_d$[GeV]	0.40	0.45	0.45	0.52	0.45	0.52	
m_s [GeV]	0.64	0.70	0.69	0.75	0.67	0.72	
ζ	0.70	0.95	0.92	0.97	0.92	0.97	
λ^2 [GeV^2]	0.25	0.1	0.1	0.1	0.1	0.1	
μ_p	2.83	2.47	2.64	2.32	2.70	2.33	2.79
μ_n	-2.37	-2.15	-2.32	-2.08	-2.08	-1.82	-1.91
octet masses, $M_N = 0.939$ GeV fixed							
Λ [GeV]	1.13	1.12	1.12	1.12	1.13	1.12	1.12
Σ [GeV]	1.30	1.27	1.29	1.30	1.22	1.21	1.19
Ξ [GeV]	1.37	1.37	1.39	1.36	1.37	1.33	1.32

TABLE II. The six parameter sets of the model investigated here and the respective results for the nucleon magnetic moments and the octet masses. Calculations using the first four sets involve only scalar diquarks, whereas the sets V and VI also include axialvector diquarks. The parameter ζ determines the diquark mass parameter (scalar and axialvector), $m_d = \zeta(m_a + m_b)$, with the mass parameters $m_{a,b}$ of its constituent quarks. The parameter λ determines the width of the diquark amplitudes, see eq (18). For set I the corresponding shape of the amplitudes was chosen to be a quadrupole ($n = 4$), for the other sets we fixed it to be a dipole ($n = 2$).

included comes considerably closer to the experimental values than in a calculation that omits these degrees of freedom (sets I–IV). As explained in ref. [6], increasing the strength of axialvector correlations in the proton forces the ratio G_E/G_M to bend to lower values. This also suggests that in order to precisely reproduce the empirical result we would need an even slightly larger axialvector coupling than the assumed $g_a/g_s = 0.2$.

All sets predict the maximum of the neutron electric form factor to lie between 0.025 and 0.04. This is only about half the value extracted from recent experiments [27,28]. This form factor is a result of delicate cancellations between the contributions from the individual diagrams shown in figure 3. Hence it is quite sensitive to small changes in the parameters. Within this model approach improved descriptions for this form factor can be found in refs. [13,6].

In a previous study [6] that employed free quark and diquark propagators we were unable to reproduce the nucleon magnetic moments and the Δ mass simultaneously. The kinematical binding of the Δ required a large constituent quark mass, $m_q = 0.43$ GeV, which in turn decreased the magnetic moments (in magnitude). Furthermore the use of free propagators enforced moderate axialvector diquark contributions (about 25%) to properly describe the ratio G_E/G_M of electric and magnetic form factors for Q^2 up to 2GeV^2. In contrast, the introduction of dressing functions for the quark–photon vertex (26,28) allows us to choose rather large up quark mass parameters around $m_u = 0.45$ GeV and still obtain a proton magnetic moment that agrees with experiment reasonably well.

Let us briefly reflect on the accuracy of our calculations. Due to the Monte–Carlo integration of the diagrams given in part b) of figure 3 (with $7.5 \cdot 10^5$ grid points for sets I-IV and $4 \cdot 10^5$ grid points for sets V and VI) the absolute numerical error for μ_p is 0.02 and for
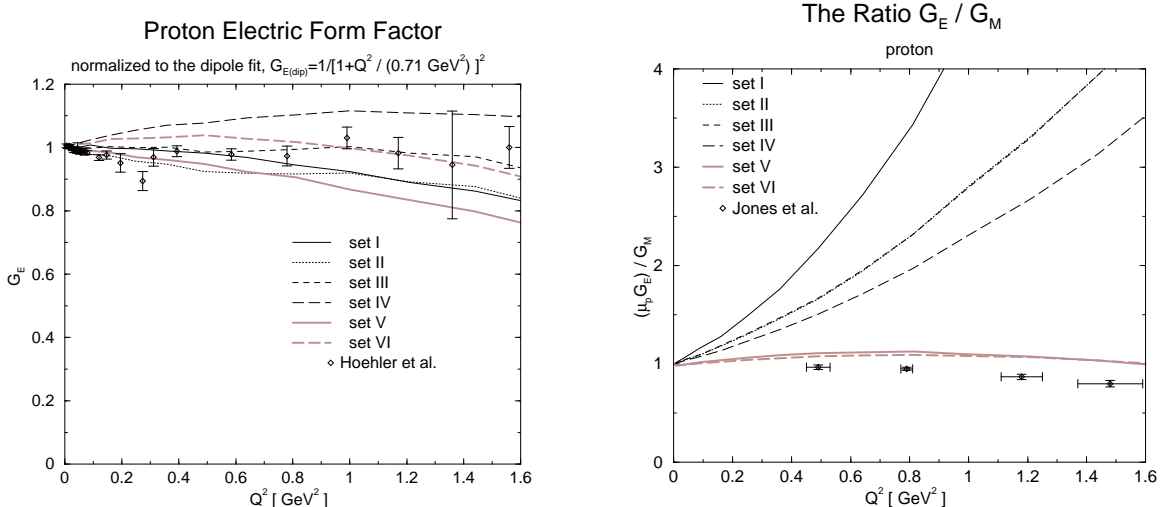
FIG. 9.   Left panel: Proton electric form factor normalized to the dipole fit. The experimental data are taken from ref. [25]. Right panel: The ratio $(\mu_p G_E)/G_M$ for the proton with the experimental data published in ref. [26].

μ_n it is 0.03. The statistical error for the electric form factor is below 0.002 up to momentum transfers of 1.7GeV^2. For the sets IV and VI a systematic relative error in the electromagnetic form factors is found that increases slowly to about 5 % at $Q^2 = 1.7\text{GeV}^2$. Furthermore, we used an expansion in Chebyshev polynomials for wave and vertex functions because this expansion can be unambiguously continued to complex arguments. Upon employing analytical propagators we have obtained identical results when using the approaches wherein either the wave functions Ψ or the vertex functions Φ must be continued analytically [13]. For non–analytic propagators, the corresponding solutions of the Bethe–Salpeter equation are non–analytic as well. Thus the analytic continuation produces errors which can be estimated by comparing the calculations using wave functions or vertex functions. In order to restrict the resulting discrepancy to below 5%, we have to choose $d > 5$ and rather large quark and diquark mass parameters. This then leads to nucleon solutions of the Bethe–Salpeter equation that resemble an analytic function in the kinematic domain needed for the ongoing computation.

B. Strong Form Factors

Above we have utilized baryon properties to determine the model parameters that enter the Bethe–Salpeter problem. Furthermore the meson–quark vertex is governed by the appropriate Ward–Takahashi identity. Finally the meson–diquark coupling constants κ_{sa} and κ_{aa} in eqs (30) and (31) have already been determined in ref. [6]. Thus we are now completely prepared to compute the loop–integrals like that in eq (32) and that appear in figure 4. Subsequently we may extract $g_{\pi NN}$ and $g_{KN\Lambda}$.

There have been numerous experimental efforts to determine the strong form factors. An extended discussion of the phenomenological value of $g_{\pi NN}$ and a comprehensive list of related references is provided in ref. [29]. Mainly the quoted discrepancies are subject to different analysis of available data. For the purpose of the present work it is sufficient to

know that the quoted data are of the order $g_{\pi NN} \approx 14$. Unfortunately the measurements of $g_{KN\Lambda}$ have not yet reached a satisfactory accuracy. The authors of [30] have extracted $|g_{KN\Lambda}(Q^2 = -M_K^2)| = 13.7 \pm 0.9$ from the LEAR–data; but other analysis have partially yielded quite different results [31,32].

In figure 10 we display the numerical results for the $g_{\pi NN}(Q^2)$ and $g_{KN\Lambda}(Q^2)$. Both form factors have been calculated in the Breit–frame. This frame is peculiar because for different masses of the initial and final baryons a numerically save treatment induces a lower bound $(Q^2 \geq \Lambda_{\mathrm{BF}}^2 = M_\Lambda^2 - M_N^2 \approx 0.4 \mathrm{GeV}^2)$ for the momentum, Q, of the coupling meson. In the case of $g_{KN\Lambda}$ we have fitted the computed form factor to rational functions and extrapolated those functions to $Q^2 \to 0$. The resulting coupling constants are shown in table III. For the special case $Q^2 = 0$ we have verified that this treatment yields the same result as a calculation in the lab–frame.

For both form factors we observe a qualitative difference between calculations with or without axialvector diquarks included. Whereas for all parameter sets with only scalar diquarks the computed pion–nucleon form factor very well reproduces the experimental data, we find that for those sets that include axialvector diquarks the computed form factor over-estimates the data. This could be due to the omission of subdominant amplitudes in the meson–quark vertex. We performed a rough estimate of the influence of the first subleading amplitude by using a simple parametrization and indeed found negative corrections to the pion–nucleon form factor of about 30%. Future calculations should include these contributions in a selfconsistent way. On the other hand in each of the subsets (I–IV) and (V–VI), the absolute value of the couplings at $Q^2 = 0$ and the respective slope are almost independent of the parameter sets and even of the propagator type. To further analyze the structure of the form factors we have disentangled the various contributions in figure 11. This figure shows that at small positive Q^2 the contribution from the coupling of the meson to the scalar quark is clearly dominating, whereas for larger momenta the diquark contributions take over.

As the form factors serve as input for later calculations we have conveniently fitted our numerical results to rational functions allowing, however, for a non–integer exponent,

$$g_{\phi BB'}(Q^2) = g_{\phi BB'} \left(\Lambda_{\mathrm{BF}}^2 \right) \left(\frac{\Lambda^2 + \Lambda_{\mathrm{BF}}^2}{\Lambda^2 + Q^2} \right)^\rho . \tag{43}$$

The result of this procedure are summarized in table III. To compare with results of other model calculations we have additionally fitted our results to monopole form factors. This has yielded scales Λ between $200 - 300 \mathrm{MeV}$ for the parameter sets with only scalar diquarks and scales around $500 \mathrm{MeV}$ for the sets including axialvector diquarks. As can be seen from figure 11 the additional contributions fall substantially slower than the scalar diquark one and become dominant for large Q^2. This effect can be interpreted as 'hardening' of the form factor. In agreement with the results from ref. [8] our form factors are much softer than those usually substituted in one–boson–exchange potential models for production processes. Those empirical scales for the monopole form are larger than $1300 \mathrm{MeV}$ [33]. However, other theoretical approaches, *e.g.* lattice measurements or QCD–sum rule calculations indicate a monopole behavior with much smaller scales, *cf.* ref. [34] and references therein.

Our prediction for $g_{KN\Lambda}(Q^2 = 0)$ is comparable to those found of QCD-sum rule or Skyrme model calculations but somewhat smaller than the chiral bag model result, *cf.* ref. [35] and references therein. Extrapolating our $g_{KN\Lambda}(Q^2)$ to the kaon mass shell

diquark:	I	II	III	IV	V	VI	expt.
		scalar			scalar and axialvector		
propagator type (f_i)	2	1	1	3	1	3	
$g_{\pi NN}$	14.0	13.4	14.3	14.0	18.2	17.5	13.4
exponent	7.8	5.1	5.1	5.2	1.4	1.6	
scale [MeV]	1327	1106	1132	1252	650	778	
$g_{KN\Lambda}$	7.98	7.39	8.25	8.12	11.97	10.23	
exponent	10.6	5.9	5.8	6.4	1.3	2.0	
scale [MeV]	1786	1368	1391	1554	642	950	

TABLE III. Numerical results for the absolute values of the couplings $g_{\pi NN}$ and $g_{KN\Lambda}$ at zero squared momentum and for the best rational fits to the curves. The parameter sets are defined in table II. The entries 'exponent' and 'scale' refer to the variables ρ and Λ in the fit (43).
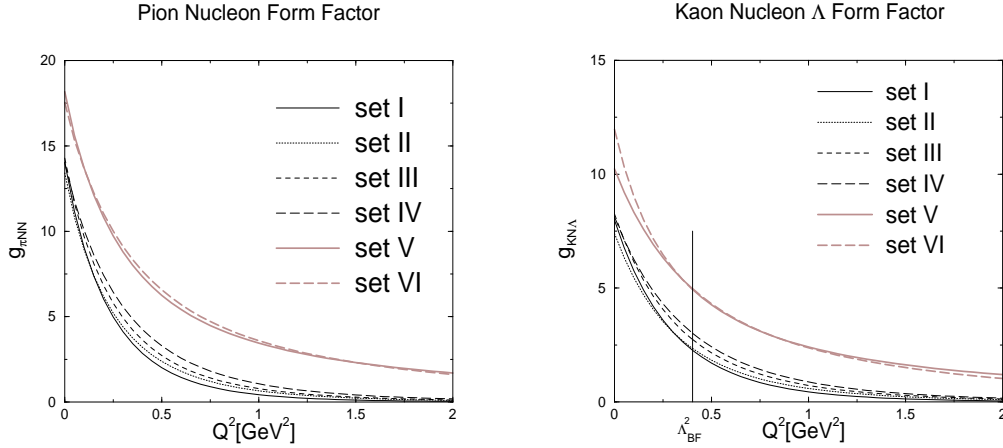

FIG. 10. The model prediction for the strong form factors $g_{\pi NN}$ and $g_{KN\Lambda}$. The parameter sets (I–VI) are defined in table II. For $g_{KN\Lambda}$ the results in the region $Q^2 < \Lambda^2_{\rm BF}$ are obtained from a rational fit (see text).

$Q^2 = -M_K^2$ yields values in the range $16.3 \leq g_{KN\Lambda} \leq 19.3$. This is slightly above the ballpark of the numbers extracted from experiment [30].

The comparison between $g_{\pi NN}$ and $g_{KN\Lambda}$ suggests three different scenarios of $SU(3)$-flavor symmetry breaking that are illustrated in figure 12. The most obvious symmetry breaking stems from different quark mass parameters $m_u \neq m_s$. Secondly, due to the flavor algebra the process in which the axialvector diquark acts as a spectator, only contributes to $g_{\pi NN}$. Finally there are different decay constants $f_K \neq f_\pi$ that factorize in the meson–quark vertices. These three effects cause $g_{KN\Lambda}(Q^2) < g_{\pi NN}(Q^2)$ independently from the type of the propagator or adopted model parameters. We see from figure 12 that at moderate and large Q^2 the different decay constants dominate the symmetry breaking effects. For small Q^2 the mass differences are essential.
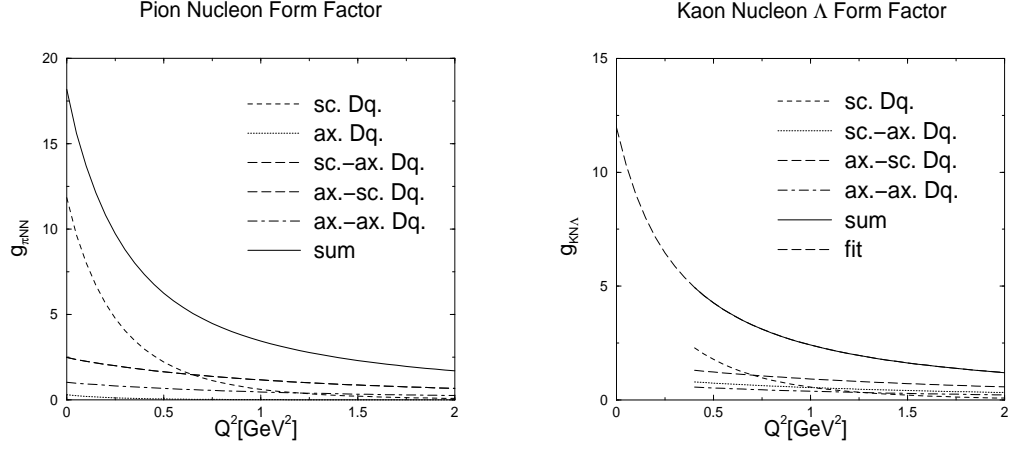
Pion Nucleon Form Factor

Kaon Nucleon Λ Form Factor

FIG. 11.   The distinct contributions to the form factors $g_{\pi NN}$ and $g_{KN\Lambda}$ calculated using parameter set V.
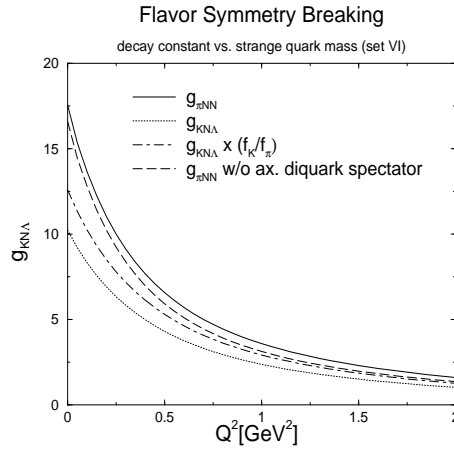
Flavor Symmetry Breaking

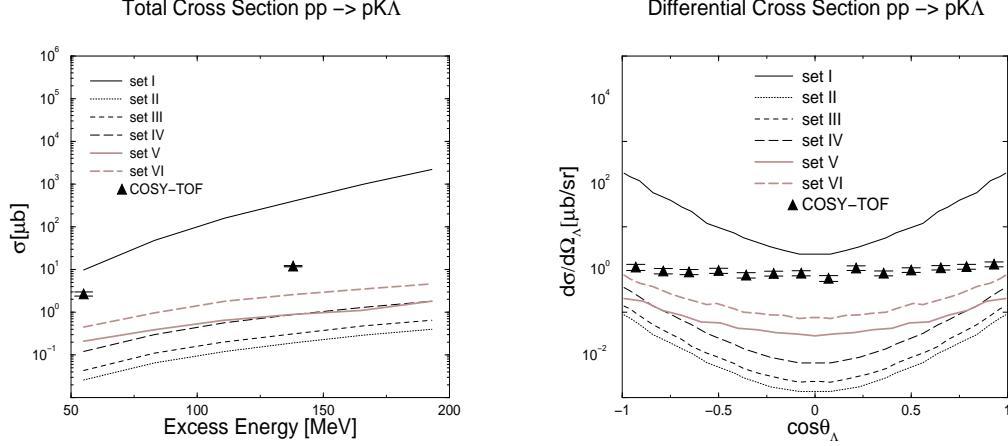FIG. 12.   Analysis of flavor symmetry breaking in $g_{KN\Lambda}$.

FIG. 13. Total and differential cross section of the process $pp \rightarrow pK\Lambda$. The differential cross section (right panel) is considered at an excess energy of $138\,\mathrm{MeV}$.

C. Associated Strangeness Production

The COSY–TOF collaboration has measured the cross section and the polarization for $pp \rightarrow pK\Lambda$ at $55\,\mathrm{MeV}$ and $138\,\mathrm{MeV}$ above threshold [36]. In addition there are also data for the depolarization tensor D_{NN} from the DISTO collaboration at SATURNE II at an excess energy of $E = 431\,\mathrm{MeV}$ [37]. This tensor is an especially interesting observable. Eventually D_{NN} might provide further information on the spin structure of the nucleon because it describes the transport of spin from the initial to the final states (cf. appendix C 2 for appropriate definitions).

Our numerical results for associated strangeness production are shown in figure 13. The comparison with the empirical data clearly shows that the propagator with an exponential dressing function (set I) yields unacceptable results. As discussed in section III the mechanism is that by increasing the beam momentum larger timelike momenta appear in the loop propagators and hence the cross sections suffer an exponential enhancement. This effect is most strongly pronounced at forward and backward angles in the differential cross section.

All propagators that do not involve the exponential dressing function underestimate the cross section for $pp \rightarrow pK\Lambda$ considerably. Only the parameter set VI can be considered to be at the right order of magnitude. Generally we find that the inclusion of axialvector diquarks improves the agreement with the data. This is not only the case for the total cross sections but also for the shape of the differential ones. The huge dip that arises for the parameter sets I-IV at directions perpendicular to the beam axis is considerably damped by the axialvector diquark contributions although it is still too deep.

The two distinct contributions to the cross section that can be characterized as being associated with pion or kaon exchange (cf. figure 8) lead to significant interference cancellations for the depolarization tensor D_{NN}. The kaon exchange processes generate the outgoing Λ in the form factor part of the diagrams. Here the γ_5-structure of the kaon vertex leads to a spin flip from the incoming proton to the Λ because of parity conservation. Therefore kaon exchange diagrams provide negative contributions to the polarization tensor. In the pion exchange diagrams, however, the outgoing Λ is generated by the handbag part of the diagram. If both mesons were on–shell a spin flip of the quarks at each vertex would result in parallel
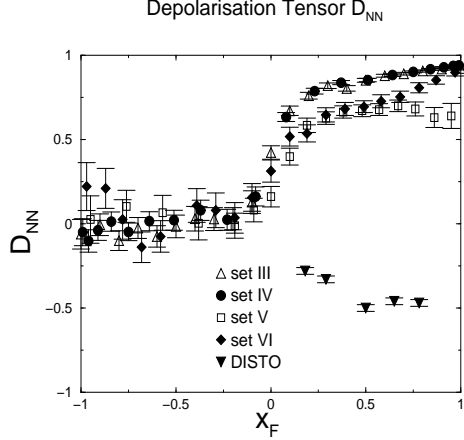
27

Depolarisation Tensor D_{NN}

FIG. 14. The depolarization tensor D_{NN} as a function of the Feynman variable x_F which measures the ration of the actual momentum of the Λ projected onto beam direction divided by the greatest possible one. The error bars on our numerical results represent the statistical error of the Monte Carlo integration.

spins of the incoming proton and the outgoing Λ. This would be a positive contribution to D_{NN}. Due to the off–shellness of the exchanged meson some small negative contributions arise. The actual magnitude depends on the particular kinematical situation considered. In essence, the depolarization tensor is controlled by the size of pion and kaon exchange contributions and in particular by the phases of the diagrams. These phases are completely controlled by the kinematics of the process. We note that in other model calculations these phases are either adjusted [38] or interference terms were completely omitted [39].

For large negative values of the Feynman–parameter x_F the outgoing Λ is dominantly produced by the unpolarized target proton. This causes the depolarization tensor to vanish. According to figure 14 our model calculations reproduce that feature. For $x_F > 0$ we obtain a sizable and positive depolarization tensor. This results from the fact that the leading contribution to the process stems form the diagram #1 in figure 8. Here the pion couples to the quark while the diquark acts as spectator. As discussed above such diagrams mainly produce Λ–spins that are parallel to the spin of the incoming proton. On the contrary the experimental results suggest that the main contribution should stem from kaon exchange [37]. We note, however, that this obvious discrepancy between theory and experiment has been found in other model calculations as well, *cf.* refs. [39], [40].

D. Kaon Photoproduction

Here we will discuss our numerical results for the process $\gamma p \to K\Lambda$. The technical details that enter this calculation are given in appendix C.

In figure 15 we display the total cross section $\sigma(\gamma p \to K\Lambda)$ as a function of the photon energy E. We observe that the parameter sets (II–IV) predict cross sections that are comparable with the experimental data. These model calculations do not include axialvector diquarks. Once these degrees of freedom are taken into account (sets V and VI), the cross–section is overestimated by about a factor four. For the five sets II–VI we find that the total cross section is strongly dominated by the kaon–exchange diagram (*cf.* figure 7) while

28

the handbag–type diagrams can almost be neglected.[8] As only a single diagram contributes interference does not occur and it is obvious that the model calculations do not reproduce the dip in the energy region $1.1\text{GeV} \leq E \leq 1.4\text{GeV}$. Tuning the model propagators such that the two diagrams are of equal importance this dip could be reproduced [24]. As it has
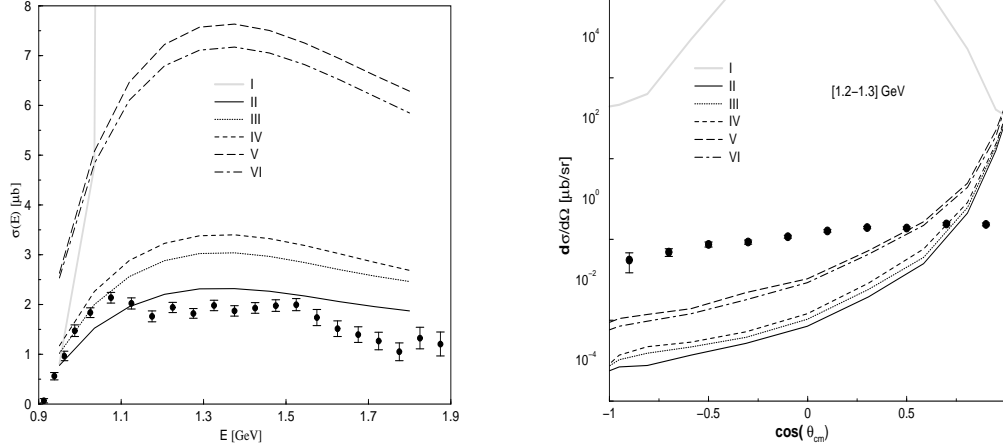

FIG. 15. The total cross section for kaon photoproduction as a function of the incident photon momentum E (left panel) and the differential cross section for kaon photoproduction averaged in the energy bin $[1.2, 1.3]\text{GeV}$. The parameter sets (I-VI) are defined in table II. The experimental data are taken from ref. [22].

been the case for the associated strangeness production we find that utilizing an exponential dressing function (set I) widely overestimates the experimental data. In this case actually the handbag diagrams dominate while the kaon exchange contributions are comparatively tiny. Figure 15 clearly shows that the large disagreement of the model results with the data certainly is not a fine–tuning problem. Rather we must conclude that the comparison with data rules out propagators that strongly rise in the timelike region as the one dressed by an exponential function does. Contrary to the case considered above the kaon exchange diagram exceeds the handbag diagram by almost one order of magnitude for the parameter sets II–IV. Possible corrections from subleading meson amplitudes in the kaon–quark vertex might decrease the strength of the kaon–nucleon–Λ form factor in a similar fashion as they do for the pion–nucleon form factor.

In figure 15 we also present the differential cross section in the energy interval $1.2\text{GeV} \leq E \leq 1.3\text{GeV}$ as a function of the angle between the momenta of the initial proton and the final kaon in the center of mass frame, *cf.* appendix C. Although the model calculations reproduce the empirical increase of the differential cross section as $\cos\theta_{cm}$ goes from minus to plus unity, the increase appears to be overestimated. For those parameter sets (II–VI) for which the resulting cross sections are dominated by the kaon exchange diagrams the predicted differential cross sections turn out too small in the backward scattering region while they are too big in the opposite direction. As a result the total cross section agrees with the empirical data reasonably well. Again, the exponential type propagators yield

---

[8]It is interesting to note that even for the handbag diagram alone results obtained with a Ball-Chiu or bare photon quark vertex, respectively, differ by at most a few percent.

differential cross sections that are way off the data and we repeatedly conclude that this type of propagators is ruled out.

We have also computed the asymmetries that are defined in eqs (C14)–(C16). We find that they essentially vanish for the model propagators that we consider reasonable, *i.e.* sets II–VI. Although the model calculation correctly predicts that the polarized photon asymmetry Σ, see eq (C16), is positive for $\cos\theta_{\mathrm{cm}} < 0$ and negative otherwise, the absolute values are off by several orders of magnitude. Only when substituting propagators that are characterized by the exponential dressing function the predicted asymmetries roughly agree with the empirical data. However, we have discarded already that propagator for other reasons given above.

VI. CONCLUSIONS

In this paper we have considered baryons as fully relativistic bound states of quarks and separable quark–quark correlations, *i.e.*, diquarks. The main purpose of this study has been to utilize empirical information in order to restrict the structure of the propagators that model confined quarks and diquarks. These propagators enter the four–dimensional Bethe–Salpeter equations from which we have computed the mass eigenvalues and wave functions that are associated with physical baryons.

The full covariance of the model wave functions allows us to unambiguously calculate form factors up to momentum transfers of several GeV. For spacelike momenta the empirical form factors can be very well reproduced with tree–level quark and diquark propagators [6]. On the other hand the description of processes involving timelike momenta is obscured by the presence of quark thresholds in the tree–level propagators. Of course, these thresholds are unphysical and reflect the absence of confinement. It is thus appropriate to modify these tree–level propagators in order to implement the confinement phenomenon. In this framework we have considered three qualitatively different cases: In the first case, the tree–level poles at timelike real p^2 have been traded for a pair of complex–conjugate poles. In this case the imaginary parts (and therefore thresholds) cancel. In the second scenario, the pole on the timelike real p^2 axis has been screened at the expense of an essential singularity for infinite timelike momenta. In the third case, we have emphasized the issue that the propagators should equal the tree–level ones for all complex values of p^2 as $|p^2| \to \infty$. Together with the condition that no poles occur this property enforces a non–analytic form. We have then investigated the phenomenological implications of either of these forms rather than attempting to precisely reproduce the experimental data. Obviously, those processes are most interesting whose computation involves timelike momenta of the order of one GeV entering the model propagators. In diquark models the flavor algebra alleviates the calculation of processes with a Λ hyperon in the final channel. We have therefore focused on kaon photoproduction and associated strangeness production with the photoproduction being, at least in principle, more sensitive to timelike momentum transfers.

The model parameters have been fixed by fitting the baryon spectrum and the nucleon electromagnetic form factors. Both, the results for the magnetic moments of the nucleon and those for the ratio G_E/G_M show that it is important to include contributions from the axialvector diquark. The strong form factors $g_{\pi NN}(Q^2)$ and $g_{KN\Lambda}(Q^2)$ for spacelike momenta $Q^2 > 0$ depend on the amount of admixture of axialvector diquarks in the baryon wave

functions. Our numerical result for $g_{\pi NN}(0)$ using both, scalar and axialvector diquarks, overestimates the empirically determined value by approximately 30%. A possible reason for this discrepancy is the omission of subleading amplitudes in the pion–quark vertex. Future calculations should therefore include these contributions and the ones from the kaon–quark vertex as well. In any event, all these observables are almost insensitive to the specific structure of the propagators. Therefore they do not provide an adequate tool to distinguish between different parameterizations of the confinement phenomenon.

The production processes, on the other hand, strongly depend on the form of the propagators in the timelike region. In particular we have observed that the class of propagators that is characterized by an exponential growth for large timelike momenta overestimates the cross sections by orders of magnitude. We have associated this failure to the dominance of the handbag–type diagram. Apparently any quark propagator that for timelike momenta is significantly more enhanced than the tree–level one immediately implies the dominance of this diagram. The obvious conclusion is that those propagators should be discarded. The other two forms of the propagators have the potential to describe the data reasonably well. As mentioned, we have omitted the so far undetermined subleading contributions in the kaon exchange diagram that dominates the kaon photoproduction amplitude. From the discussion of the pion form factor we have sufficient reason to believe that the inclusion of such contributions will favor parameter sets that contain axialvector diquarks. Although the non–analytic form for the propagator could not be ruled out by quantitative arguments we nevertheless think it should be discarded, because it poses several fundamental problems related with gauge and translational invariance which we have detailed in the text. Therefore propagators that are characterized by pairs of complex conjugated poles seem to be best suited for further studies.

APPENDIX A: FROM THE RELATIVISTIC THREE–QUARK PROBLEM TO THE DIQUARK–QUARK MODEL

The six–point function $G(x_i, y_i) = \langle 0|T \prod_{i=1}^{3} q(x_i)\bar{q}(y_i)|0\rangle$ represents the starting point for our study of the relativistic three–quark problem. Here the variables x_i and y_i not only represent the space–time coordinates but also include the discrete labels color, spin, and flavor. The six–point function obeys the Dyson equation

$$G = G_0 + G_0 \otimes K \otimes G\,. \tag{A1}$$

The entries of the Dyson equation (A1) are the disconnected six–point function G_0 that describes the free propagation of three quarks and the three–quark scattering kernel K that contains all two– and three–particle irreducible diagrams. The symbol "$\otimes$" in eq (A1) denotes summation/integration over all independent internal coordinates and labels. Unless

explicitly stated otherwise we will henceforth work in momentum space with Euclidean metric. It is thus not necessary to introduce different symbols for momentum and coordinate space objects.

A three–particle bound state with mass M manifests itself as a pole in the six–point function at $-P^2 = M^2$ where $P = p_1 + p_2 + p_3$ is the total four–momentum of the three–quark system. We may thus parameterize the six–point function in the vicinity of the pole as

$$G(k_i, p_i) \sim \frac{\psi(k_1, k_2, k_3)\, \bar\psi(p_1, p_2, p_3)}{P^2 + M^2} \,, \tag{A2}$$

where ψ denotes the bound state wave–function. Substituting this parameterization into the Dyson equation (A1) and identifying residua, we find the homogeneous bound state equation

$$\psi = G_0 \otimes K \otimes \psi \quad \Longleftrightarrow \quad G^{-1} \otimes \psi = 0 \,. \tag{A3}$$

Despite its simple appearance this equation is infeasible as neither all two– and three–particle graphs, K, nor the fully dressed quark propagator, that is contained in G_0, are known. We will have to resort to approximations that render the problem tractable and *a posteriori* validate these approximations from the resulting bound state properties.

The problem greatly simplifies when discarding all three–particle irreducible graphs from the interaction kernel K. The kernel may then be written as the sum of three two–quark interaction kernels,

$$K = K_1 + K_2 + K_3 \,. \tag{A4}$$

We adopt the notation that the subscript of K_i refers to the spectator quark q_i. The respective interacting quark pair is (q_j, q_k) with the three labels (i, j, k) being a cyclic permutation of $(1, 2, 3)$. These two–quark interaction kernels govern the Dyson equation for the two–quark correlation functions, g_i:

$$g_i = G_0 + G_0 \otimes K_i \otimes g_i \,. \tag{A5}$$

As the appearance of the free six–point function G_0 suggests we have defined both g_i and K_i in the three–quark space. This is easily accomplished by attaching the propagator[9] S_i of the spectator quark to g_i and its inverse S_i^{-1} to K_i. Expressing eq (A5) as $G_0 \otimes K_i = 1 - G_0 \otimes g_i^{-1}$ allows us to replace any of the three operators $G_0 \otimes K_i$ in the bound state equation (A3),

$$\psi = \left(1 - G_0 \otimes g_i^{-1}\right) \otimes \psi + G_0 \otimes (K_j + K_k) \otimes \psi \quad \Longleftrightarrow \quad \psi = g_i \otimes (K_j + K_k) \otimes \psi \,. \tag{A6}$$

To further elaborate this form of the bound state equation we define the matrix $\hat{t}_i$ via

---

[9]In the framework of these integral equations we factorize the momentum conservation $\langle p_i | S_i | p_i' \rangle = (2\pi)^4 S(p_i) \delta^4(p_i' - p_i)$. Here $S(p)$ is the ordinary Dirac propagator while S_i refers to an operator in functional space. We adopt analogous conventions for the other operators.
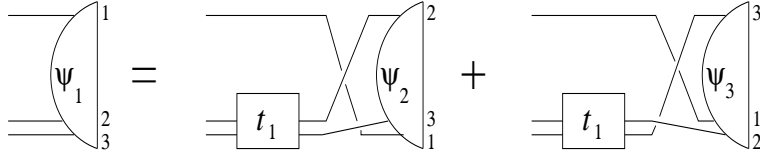
FIG. 16. The Faddeev bound state equation for the component ψ_1. The equations for ψ_2 and ψ_3 follow by cyclic permutation of the particle indices.

$$g_i = G_0 + G_0 \otimes \hat{t}_i \otimes G_0 \ . \tag{A7}$$

This reflects the amputation of the external quark legs from g_i after having separated the non–interacting contribution. As already mentioned we carry along factors of the quark propagators and its inverse to formulate the problem in the three–quark space. For later convenience we therefore define

$$t_i = \hat{t}_i \circ S_i \tag{A8}$$

with the additional factor removed. We have introduced the symbol "$\circ$" to denote simple multiplications without any contractions because the so–combined operators act on different quarks. Finally we introduce the Faddeev components ψ_i by

$$\psi_i = G_0 \otimes K_i \otimes \psi \ . \tag{A9}$$

Upon rewriting the definition (A7) for $\hat{t}_i$ as $g_i \otimes G_0^{-1} = 1 + G_0 \otimes \hat{t}_i$ we find the bound state equation $\psi = \psi_j + \psi_k + G_0 \otimes \hat{t}_i \otimes (\psi_j + \psi_k)$ and thus

$$\psi_i = G_0 \otimes \hat{t}_i \otimes (\psi_j + \psi_k) = (S_j \circ S_k) \otimes t_i \otimes (\psi_j + \psi_k) \ . \tag{A10}$$

These are the famous Faddeev bound state equations relating the Faddeev component ψ_i to ψ_j and ψ_k. The graphical representation of these equations is shown in figure 16. These equations embody the full two–quark correlation function t_i instead of the kernel K. The relativistic Faddeev equations are a set of coupled four–dimensional integral equations and represent a considerable simplification over the original eight–dimensional integral equation problem defined in eq (A3). Unfortunately the Faddeev components ψ_i still depend on the two relative momenta between the three quarks. Expanding these components in Dirac space [41] yields an intractable number of coupled integral equations. We therefore further simplify the bound state problem. Denoting the incoming and outgoing momenta by respectively k_i and p_j we assume that the two–quark correlations t_i do <u>not</u> depend on any of the scalar products $k_i \cdot p_j$ that connect momenta of the incoming and outgoing channels. This assumption allows us to expand t_i in terms of separable correlations in the two–quark subspace that is characterized by $j, k \neq i$ and $j \neq k$,

$$t_i(k_j, k_k; p_j, p_k) = \sum_{a,a'} \chi_i^a(k_j, k_k) \, D_{a,a'}(k_j + k_k) \, \bar{\chi}_i^{a'}(p_j, p_k) \ . \tag{A11}$$

We call these separable correlations "diquarks" and comprise the various types together with their discrete quantum numbers within the label a. Note that the propagator $D_{a,a'}(k_j + k_k)$

is diagonal in the discrete quantum numbers a and a' except for the Lorentz indices for the axialvector diquark. Furthermore χ^a represents the vertex function of two quarks with a diquark. Correspondingly $\bar{\chi}^a$ denotes the conjugate vertex function. The expansion (A11) is pictured in figure 17.

In a full solution to the Faddeev problem the t_i will have to be determined from the Dyson equation for $\hat{t}_i$

$$\hat{t}_i = K_i + K_i \otimes G_0 \otimes \hat{t}_i \ , \tag{A12}$$

that follows from eq (A5) and involves the kernel components K_i. Rather than determining these vertices and the diquark propagators from that Dyson equation we will adopt phenomenologically motivated parameterizations for these quantities.

Upon the separability assumption for the two–quark correlations we continue to formulate a relativistic description of baryons based on the Faddeev equations (A10). In this approach it is advantageous to introduce an effective vertex function, ϕ_i^a, for the interaction of the baryon with the quark and the diquark. This vertex function depends only on the momentum of the spectator quark, p_i, and the momentum, $p_j + p_k$ of the diquark quasiparticle. Eventually this can be reexpressed as a dependence on the relative momentum between quark and diquark, $\bar{p}_i$ as well as the total momentum P: $\phi_i^a = \phi_i^a(\bar{p}_i, P)$. These dependencies are further detailed in refs. [42,43]. In contrast to the non–relativistic formulation we have some freedom in the definition of the relative momentum. We may write

$$\bar{p}_i = p_i - \eta P = (1 - \eta)p_i - \eta(p_j + p_k) \ , \tag{A13}$$

where the parameter η parameterizes the partition of this momentum among the constituents. Of course, physical observables like the mass of the bound state or form factors do not depend on this parameter (up to numerical uncertainties). The superscript in ϕ_i^a selects a diquark content, a, that builds a baryon together with the quark of species q_i. A suitable *ansatz* for the Faddeev components ψ_i then reads

$$\psi_i^{\alpha\beta\gamma} = S_i^{\alpha\alpha'} S_j^{\beta\beta'} S_k^{\gamma\gamma'} \sum_{aa'} \chi_{i,\beta'\gamma'}^a \ D_{aa'} \phi_{i,\alpha'}^{a'} \ , \tag{A14}$$

where we have made the quark labels explicit. As usual, we sum over doubly appearing indices. The quark label i fixes the diquark indices (jk). The momentum routing follows these indices as well as the diquark labels a and a'. For further guidance we have visualized this *ansatz* in figure 18. Noting that $G_0 = S_i \circ S_j \circ S_k$ we find the coupled integral equations for the effective vertex functions

$$\phi_{i,\alpha}^a = \sum_{bb'} \left[\bar{\chi}_{i,\beta\gamma}^a S_k^{\gamma\gamma'} \chi_{j,\gamma'\alpha}^b \right] \left[D_{bb'} S_j^{\beta\beta'} \phi_{j,\beta'}^{b'} \right] \quad + \quad (j \longleftrightarrow k) \ , \tag{A15}$$

FIG. 17. The separable matrix t_1. Also indicated is the amputation of the external legs in the quark propagators.
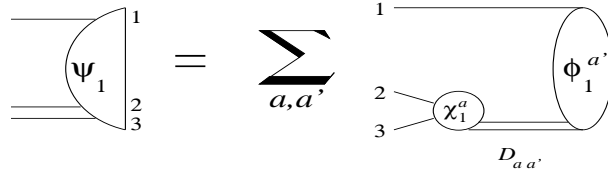
FIG. 18. The *ansatz* (A14) for the Faddeev component ψ_1 of the bound state wave function ψ using effective baryon-quark-diquark vertex functions ϕ_1^a.

when inserting the *ansatz* (A14) together with the diquark parameterization (A11) into the Faddeev equations (A10). In deriving eq (A15) we have utilized that the quark–diquark vertex functions are antisymmetric under the exchange of the quark labels, $\chi_{i,\beta\gamma}^a = -\chi_{i,\gamma\beta}^a$. This feature is a consequence of the Pauli exclusion principle. We have arranged the terms in eq (A15) such as to exhibit the similarity with the structure of Bethe–Salpeter equations. The first term in square brackets represents a six–point function for quarks that is governed by the exchange of a single quark between a quark and a diquark. By coupling to the vertex function via the propagators for quarks and diquarks it serves as the interaction kernel that generates the Bethe–Salpeter equation for a bound state of quarks and diquarks. Thus the Bethe–Salpeter equation sums the ladder–type quark exchange diagrams between quarks and diquarks. Using the above definitions for total and relative momentum one arrives now at the Bethe–Salpeter equation (6).

APPENDIX B: DECOMPOSITION OF THE DIQUARK–QUARK BETHE–SALPETER AMPLITUDE

Here we will make explicit the full structure of the vertex functions ϕ_i^a for the case of the nucleon–quark–diquark vertex. For identical quarks the nucleon–quark–diquark vertex functions ϕ_i^a do not depend on the quark label i. The vertex functions consist of a spinor in the case of a scalar diquark ($a = 5$) and a vector–spinor in the case of an axialvector diquark ($a \equiv \mu = 1 \dots 4$). Using positive energy spinors $u(P)$ with P being the nucleon momentum, we define matrix–valued vertex functions $\Phi = \begin{pmatrix} \Phi^5 \\ \Phi^\mu \end{pmatrix}$ via

$$\phi^a(p, P) = \Phi(p, P)\, u(P) \,. \tag{B1}$$

Upon attaching quark and diquark legs to Φ we obtain the matrix–valued Bethe–Salpeter wave functions $\Psi = \begin{pmatrix} \Psi^5 \\ \Psi^\mu \end{pmatrix}$,

$$\tilde{D}(p_d) := \begin{pmatrix} D(p_d) & 0 \\ 0 & D^{\mu\nu}(p_d) \end{pmatrix} \,, \tag{B2}$$

$$\Psi(p, P) = \left[S(p_q) \circ \tilde{D}(p_d) \right] \Phi(p, P) \,. \tag{B3}$$

We demand that the nucleon Faddeev amplitude eq (A14) has positive parity and describes positive–energy states. The latter condition enforces that wave– and vertex functions are eigenfunctions of the positive–energy projector $\Lambda^+ = \frac{1}{2}(1 - i\slashed{P}/M)$, *i.e.*,

$\mathcal{S}_1$	Λ^+
$\mathcal{S}_2$	$-i\,\hat{\not{p}}_T\,\Lambda^+$
$\mathcal{A}_1^\mu$	$\hat{P}^\mu\,\Lambda^+$
$\mathcal{A}_2^\mu$	$-i\,\hat{P}^\mu\,\hat{\not{p}}_T\,\Lambda^+$
$\mathcal{A}_3^\mu$	$\frac{1}{\sqrt{3}}\,\gamma_T^\mu\,\Lambda^+$
$\mathcal{A}_4^\mu$	$\frac{i}{\sqrt{3}}\,\gamma_T^\mu\,\hat{\not{p}}_T\,\Lambda^+$
$\mathcal{A}_5^\mu$	$\sqrt{\frac{3}{2}}\left(\hat{p}_T^\mu\,\hat{\not{p}}_T - \frac{1}{3}\gamma_T^\mu\right)\Lambda^+$
$\mathcal{A}_6^\mu$	$i\sqrt{\frac{3}{2}}\left(\hat{p}_T^\mu - \frac{1}{3}\gamma_T^\mu\,\hat{\not{p}}_T\right)\Lambda^+$

TABLE IV. Basic Dirac components of the nucleon vertex function. The hat denotes normalized four–vectors, $\hat{p} = p/|p|$. For the complex on-shell nucleon momentum, we define $\hat{P} = P/iM$. The subscript "T" denotes the transversal component of a vector with respect to the nucleon momentum P, e.g. $p_T = p - (p \cdot \hat{P})\hat{P}$.

$$\Phi = \Phi\,\Lambda^+ \qquad \text{and} \qquad \Psi = \Psi\,\Lambda^+ \ . \tag{B4}$$

Using these constraints, the most general structure of Φ contains two amplitudes (scalar functions) $S_1(p,P)$ and $S_2(p,P)$ coupling to the scalar correlations and six amplitudes $A_1(p,P),\ldots,A_6(p,P)$ for the axialvector correlations within the nucleon. Explicitly,

$$\Phi^5(p,P) = \sum_{i=1}^{2} S_i(p^2, p \cdot P)\,\mathcal{S}_i(p,P) \ ,$$

$$\Phi^\mu(p,P) = \sum_{i=1}^{6} A_i(p^2, p \cdot P)\,\gamma_5\mathcal{A}_i^\mu(p,P) \ . \tag{B5}$$

The Dirac components $\mathcal{S}_1, \cdots, \mathcal{A}_6$ that obey the positive energy condition are listed in table IV. Also, these components have positive parity. We remark that the wave–function Ψ can be analogously expanded because it must obey the same constraints as Φ does. In the nucleon rest frame the individual components of Ψ are eigenfunctions of the three–quark spin and orbital angular momentum operators, respectively, when the Faddeev amplitude is expanded within the basis (B5) [7]. Thus, the amplitude S_1 describes the strength of an s–wave in the scalar channel while A_1 and A_3 represent s–waves in the axialvector channel. There also is a small d–wave component in the nucleon parameterized by A_5. All amplitudes with even labels are relativistic (lower) components associated with the above described amplitudes that have an odd label, and these flavor components are absent in a nonrelativistic description.

APPENDIX C: TECHNICAL DETAILS FOR CALCULATING PRODUCTION PROCESSES
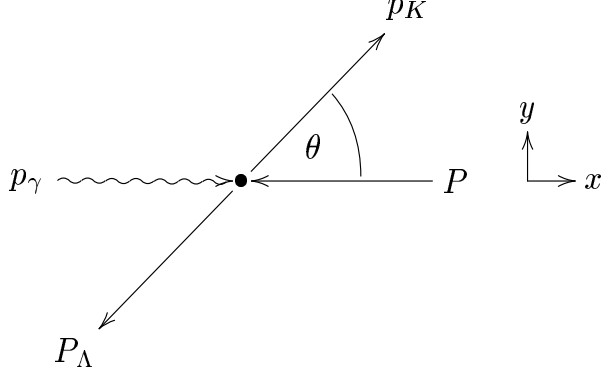
FIG. 19. Kinematics for kaon photoproduction $p\gamma \to \Lambda K$ in the center of momentum frame. The incoming proton and photon carry the momenta P and p_γ respectively. The outgoing kaon and Λ are labeled by the momenta p_K and P_Λ.

1. Kaon Photoproduction $p\gamma \to \Lambda K$

In this appendix we detail the calculation of the diagrams shown in figure 7. They provide the main contributions to the photoproduction process $p\gamma \to \Lambda K$.

We have performed the calculations in both the rest frame of the proton and in the center of momentum system (CMS). For the following discussion we choose the CMS for definiteness. The momenta are defined according to figure 19, that is

$$P = (-E, 0, 0, iE_P), \quad p_\gamma = (E, 0, 0, iE)$$
$$p_K = (|\vec{p}_K| \cos\theta, |\vec{p}_K| \sin\theta, 0, iE_K), \quad P_\Lambda = (-|\vec{p}_K| \cos\theta, -|\vec{p}_K| \sin\theta, 0, iE_\Lambda) \qquad \text{(C1)}$$

with

$$E_P = \sqrt{M_P^2 + E^2}, \quad E_K = \frac{1}{2(E + E_P)} \left((E + E_P)^2 - M_\Lambda^2 + M_K^2 \right)$$
$$|\vec{p}_K| = \sqrt{(E_K)^2 - M_K^2}, \quad E_\Lambda = \sqrt{\vec{p}_K{}^2 + M_\Lambda^2}. \qquad \text{(C2)}$$

The on–shell conditions and momentum conservation leave only two kinematical variables undetermined. These are usually chosen to be the energy E of the incoming photon and the angle θ between the spatial momenta of the photon and the outgoing kaon.

The three diagrams in figure 7 show the contributions to the transition amplitudes that we will discuss here. The uncrossed 'handbag diagram' translates into

$$A_1 = i \int \frac{d^4p}{(2\pi)^4} \left\{ \bar\Phi_\Lambda(p_f, P_\Lambda) S(p_+) \Gamma_K(q, p_+) S(q) \right\} \left\{ \Gamma_\gamma(p_-, q) S(p_-) \Phi(p, P) D(p_d) \right\} \qquad \text{(C3)}$$

with the momentum routing described in eq (38), see also figure 7. The crossed 'handbag diagram' corresponds to the expression

$$A_2 = i \int \frac{d^4p}{(2\pi)^4} \left\{ \bar\Phi_\Lambda(p_f, P_\Lambda,) S(p_+) \Gamma_\gamma(q, p_+) S(q) \right\} \left\{ \Gamma_K(p_-, q) S(p_-) \Phi(p, P) D(p_d) \right\}. \qquad \text{(C4)}$$
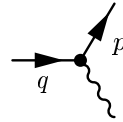
The definitions for q and p_+ have changed as compared to the momentum routing for the amplitude A_1 given in eq (38). In eq (C4) we have instead:

$$q = p_- - p_K \quad \text{and} \quad p_+ = q + p_\gamma \,, \tag{C5}$$

with all other momentum definitions unchanged. The amplitude corresponding to the tree level diagram arising from kaon exchange is given by

$$A_3 = (\bar{u}_\Lambda [g_{KN\Lambda} \gamma_5] u_p) \frac{1}{q^2 + M_K^2} (\Gamma^\nu \epsilon_\nu) \,. \tag{C6}$$

Here $g_{KN\Lambda}$ represents the strong form factor that has been discussed in subsection II C and M_K is the kaon mass. The photon polarization is denoted by ϵ_ν while Γ^ν refers to kaon–photon vertex containing the electromagnetic kaon form factor

$$= \Gamma^\nu(q, p) = (q^\nu + p^\nu) F_{K^+}((p - q)^2) \,. \tag{C7}$$

For the purpose of the present investigation it is sufficient to parameterize the kaon charge form factor with a monopole such that the phenomenological value of the kaon radius, $\langle r_{K^+}^2 \rangle = (0.34 \pm 0.05)\text{fm}^2$, is reproduced: $F_{K^+}(Q^2) = 1/(1 + Q^2/(0.84\text{GeV})^2)$.

In section III we have already reflected on the Bethe–Salpeter formalism in Euclidean space. We choose the loop momentum p to be real, thus the temporal components of the external momenta in eqs (C1)–(C1) are purely imaginary. Hence the relative momentum p_f as given in (38) is complex. Since the solution of the Bethe–Salpeter equation provides the vertex function Φ_Λ only for real relative momenta p_f, we have to extrapolate Φ_Λ to complex momenta. We fit rational functions to the vertex functions that are known at N real meshpoints. These rational functions can then easily be analytically continued. For real momenta a comparison of the fitted parameterization to the known results allows us to estimate the reliability of this treatment.

The differential cross section depends only on the energy E of the incoming photon and the angle θ between the spatial photon and kaon momenta. That is illustrated in figure 19. The differential cross section is defined with respect to the solid angle element $d\Omega_K = 2\pi d(\cos\theta)$ of the outgoing kaon:

$$\frac{d\sigma}{d\Omega_K}(E, \theta) = \frac{1}{4} \sum_{s_i, s_f} \frac{\tilde{d\sigma}}{d\Omega_K}(E, \theta) \tag{C8}$$

with

$$\frac{\tilde{d\sigma}}{d\Omega_K}(E, \theta) = \frac{\alpha}{64\pi^2} 4 M_P M_\Lambda |A_1 + A_2 + A_3|^2 \,. \tag{C9}$$

We average, respectively sum over the spins s_i, s_f of the initial and final states. The phase space factors denoted by α are given as

$$\alpha = \frac{1}{P \cdot p_\gamma} \frac{|\vec{p}_K|^2}{E_K E_\Lambda} \left| \frac{d |\vec{p}_K|}{d(E_K + E_\Lambda)} \right| \tag{C10}$$

with

$$\left| \frac{d\, |\vec{p}_K|}{d(E_K + E_\Lambda)} \right| = \left(\frac{|\vec{p}_K|}{E_K} - \frac{\hat{p}_K \cdot \vec{P}_\Lambda}{E_\Lambda} \right)^{-1}. \tag{C11}$$

Note that the right hand side of eq (C11) remains positive given that $m_\Lambda > M_K$. In the CMS the expression (C10) for α simplifies to

$$\alpha = \frac{|\vec{p}_K|}{|\vec{p}_\gamma|} \frac{1}{s}, \tag{C12}$$

where $s = (P + p_\gamma)^2 = (p_K + P_\Lambda)^2$ denotes the total center of mass energy squared. In obtaining the phase space factors (C10) we adopted the one particle normalization conditions (for Minkowski space)

$$\langle p | p' \rangle_B = 2p^0 (2\pi)^3 \delta^3(\vec{p} - \vec{p}') \quad \text{and} \quad \langle p | p' \rangle_F = \frac{p^0}{m}(2\pi)^3 \delta^3(\vec{p} - \vec{p}'), \tag{C13}$$

for bosons (B) and fermions (F). These conventions also enter the calculation of the transition amplitudes $A_i, i = 1, 2, 3$ and the normalization of the Bethe–Salpeter wave–functions.

We obtain the various asymmetries by restricting the sum in eq (C8) over the spins to two of the three non–scalar particles. We thus obtain the Λ–*polarization asymmetry*

$$P(E, \theta) = \frac{1}{4} \sum_{s_p, s_\gamma} \frac{[s_\Lambda = \uparrow] - [s_\Lambda = \downarrow]}{[s_\Lambda = \uparrow] + [s_\Lambda = \downarrow]} \tag{C14}$$

the *polarized target asymmetry*

$$T(E, \theta) = \frac{1}{2} \sum_{s_\Lambda, s_\gamma} \frac{[s_p = \uparrow] - [s_p = \downarrow]}{[s_p = \uparrow] + [s_p = \downarrow]} \tag{C15}$$

and the *polarized photon asymmetry*

$$\Sigma(E, \theta) = \frac{1}{2} \sum_{s_\Lambda, s_p} \frac{[s_\gamma = \uparrow] - [s_\gamma = \downarrow]}{[s_\gamma = \uparrow] + [s_\gamma = \downarrow]}, \tag{C16}$$

where we used the shorthand notation

$$[s_\Lambda = \uparrow] = \left. \frac{\tilde{d}\sigma}{d\Omega_K} \right|_{s_\Lambda = \uparrow} \qquad \text{etc.} \tag{C17}$$

Furthermore we denote the spins of the photon, the proton and the Λ by s_γ, s_p and s_Λ, respectively.

The total cross section is finally obtained from eq (C8) via

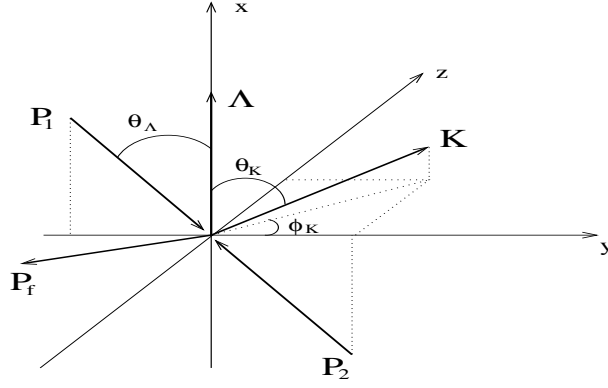$$\sigma(E) = \int_0^\pi \sin\theta \, d\theta \frac{d\sigma}{d\Omega_K}(E, \theta). \tag{C18}$$

FIG. 20. Kinematical variables for the reaction $pp \to pK\Lambda$ in the center of momentum system.

2. Associated Strangeness Production $pp \to pK\Lambda$

Again we calculate the cross section for the productions process $pp \to pK\Lambda$ in the center of momentum frame. The kinematical setup is depicted in figure (20) and amounts to the momentum routing

$$
\begin{aligned}
P_1 &= (|\vec{p}| \cos(\theta_\Lambda), |\vec{p}| \sin(\theta_\Lambda), 0, iE), \quad P_2 = (-|\vec{p}| \cos(\theta_\Lambda), -|\vec{p}| \sin(\theta_\Lambda), 0, iE), \\
K &= (K_x, |\vec{K}| \sin(\theta_K) \cos(\phi_K), |\vec{K}| \sin(\theta_K) \sin(\phi_K), iE_K), \\
\Lambda &= (\Lambda_x, 0, 0, iE_\Lambda), \quad P_f = (\vec{P}_f, iE_P),
\end{aligned}
\tag{C19}
$$

where E denotes the center of momentum energy. We have furthermore introduced

$$
E_P = 2E - E_\Lambda - E_K, \quad \Lambda_x = \sqrt{E_\Lambda^2 - M_\Lambda^2}, \quad |\vec{K}| = \sqrt{E_K^2 - M_K^2}, \quad \vec{P}_f = -\vec{K} - \vec{\Lambda}
$$

$$
K_x = \frac{E_P^2 - E_K^2 - \Lambda_x^2 + M_K^2 - M_P^2}{2\Lambda_x}, \quad \sin(\theta_K) = \sqrt{1 - \left(\frac{K_x}{|\vec{K}|}\right)^2},
\tag{C20}
$$

where all the momenta are Euclidean. There are now four independent variables left: E_Λ, E_K, θ_Λ and ϕ_K. As for $p\gamma \to K\Lambda$ we find the vertex function Γ_Λ for complex arguments by analyticly continuing a fitted rational function.

The differential cross section is given by

$$
\frac{d\sigma}{d\Omega_\Lambda} = \frac{1}{4} \sum_{s,s',r,r'} \int d\Sigma \, |\mathcal{M}_{s,s',r,r'}|^2, \quad \text{where} \quad d\Sigma = \frac{1}{128\pi^5} \frac{M_P^3 M_\Lambda}{|\vec{p}_{cm}|E} dE_K \, dE_\Lambda \, d\phi_K,
\tag{C21}
$$

with $d\Omega_\Lambda = 2\pi \, d\cos(\theta_\Lambda)$. The masses of the proton and the Λ are denoted by M_P and M_Λ while $(\vec{p}_{cm}, iE)$ represents the four vector of the total momentum in the CMS. The amplitude $\mathcal{M}_{s,s',r,r'}$ for the reaction $p\gamma \to K\Lambda$ depends on the spin orientation of the incoming and outgoing particles. In (C21) we average, respectively sum over the spin projections of the incoming and outgoing particles. The integrations over the kaon and Λ energies are constrained by the available energy, which is $2E$.

For each diagram in figure 8 and for each specific diquark content (*cf.* Table I) one has a contribution of the form

$$\mathcal{L} \left(\frac{i}{Q^2 + m_\phi^2} \right) \mathcal{H} \tag{C22}$$

to the amplitude $\mathcal{M}$. Here m_ϕ refers to the mass of the intermediate pseudoscalar meson, *i.e.* $m_\phi = M_\pi$ or $m_\phi = M_K$. The 'meson matrix element' is given by

$$\mathcal{L}_{s,s'} = \bar{u}_{s'}(P_2)\, i\gamma_5 \, g_{\pi NN}(Q^2)\, u_s(P_f) \quad \text{or} \quad \mathcal{L}_{s,s'} = \bar{u}_{s'}(P_2)\, i\gamma_5 \, g_{KN\Lambda}(Q^2)\, u_s(P_\Lambda)\,, \tag{C23}$$

depending on whether the intermediate meson is a pion or a kaon. The 'handbag part' $\mathcal{H}$ has the general structure

$$\mathcal{H} = i \int \frac{d^4 p}{(2\pi)^4} \left\{ \bar{\Phi}_\Lambda(p_f, P_f)\, S(p_+)\, \Gamma_K(p_+, q)\, S(q) \right\} \left\{ \Gamma_\pi(q, p_-)\, S(p_-) D(p_d)\, \Phi_P(p_i, P_i) \right\}. \tag{C24}$$

Here the Bethe–Salpeter amplitudes $\bar{\Phi}_\Lambda$ and Φ_P for the Λ and the proton as well as the (di)quark propagators S and D enter. The meson–quark vertices Γ_π and Γ_K are defined in eq (29).

The calculation of the amplitudes involves four dimensional loop integrations. All the momenta are Euclidean and therefore we use hyperspherical coordinates. For the inner loop of the handbag diagrams we use a Gauss–Legendre routine, whereas the phase space integration is performed with Monte–Carlo methods. Due to the considerable effort it takes to integrate eight integrals numerically the calculation could only be performed to an overall accuracy of 5% to 15%. However, we consider that sufficient for a comparison with data.

The depolarization tensor is defined as

$$D_{NN}(x_F) = \frac{a - b}{a + b} \tag{C25}$$

with the shorthand notation

$$a = \frac{d\sigma}{dx_F}(\uparrow_p\uparrow_\Lambda + \downarrow_p\downarrow_\Lambda) \quad \text{and} \quad b = \frac{d\sigma}{dx_F}(\uparrow_p\downarrow_\Lambda + \downarrow_p\uparrow_\Lambda) \tag{C26}$$

for the cross sections with different spin projections. Here x_F denotes the real momentum of the Λ scaled by the maximum value allowed by the kinematics:

$$x_F = \frac{|\vec{\Lambda}_\||}{|\vec{\Lambda}_{\|max}|}\,. \tag{C27}$$

REFERENCES

[1] C. D. Roberts and S. M. Schmidt, Prog. Part. Nucl. Phys. **45** (2000) S1 [nucl-th/0005064].

[2] R. Alkofer and L. von Smekal, Physics Reports, in press [hep-ph/0007355].

[3] R. Alkofer and H. Reinhardt, "Chiral quark dynamics," *Berlin, Germany: Springer (1995) 114 p. (Lecture notes in physcis).*

[4] H. Reinhardt, Phys. Lett. **B244** (1990) 316.

[5] R. T. Cahill, C. D. Roberts and J. Praschifka, Austral. J. Phys. **42** (1989) 129.

[6] M. Oettel, R. Alkofer and L. von Smekal, Eur. Phys. J. **A8** (2000) 553 [nucl-th/0006082]; *see also:* G. Hellstern, R. Alkofer, M. Oettel and H. Reinhardt, Nucl. Phys. **A627** (1997) 679 [hep-ph/9705267]; M. Oettel and R. Alkofer, Phys. Lett. **B484** (2000) 243 [hep-ph/0001261].

[7] M. Oettel, G. Hellstern, R. Alkofer and H. Reinhardt, Phys. Rev. **C58** (1998) 2459 [nucl-th/9805054].

[8] J. C. Bloch, C. D. Roberts and S. M. Schmidt, Phys. Rev. **C61** (2000) 065207 [nucl-th/9911068].

[9] J. C. Bloch, C. D. Roberts, S. M. Schmidt, A. Bender and M. R. Frank, Phys. Rev. **C60** (1999) 062201 [nucl-th/9907120].

[10] B. Blankleider and A. N. Kvinikhidze, Phys. Rev. **C62** (2000) 039801 [nucl-th/9912003].

[11] M. Stingl, Z. Phys. **A353** (1996) 423 [hep-th/9502157].

[12] G. V. Efimov and M. A. Ivanov, "The Quark confinement model of hadrons," *Bristol, UK: IOP (1993) 177 p.*

[13] M. Oettel, M. Pichowsky and L. von Smekal, Eur. Phys. J. **A8** (2000) 251 [nucl-th/9909082].

[14] A. Bender, C. D. Roberts and L. von Smekal, Phys. Lett. **B380** (1996) 7 [nucl-th/9602012].

[15] G. Hellstern, R. Alkofer and H. Reinhardt, Nucl. Phys. **A625** (1997) 697 [hep-ph/9706551].

[16] U. Zückert, R. Alkofer, H. Weigel and H. Reinhardt, Phys. Rev. **C55** (1997) 2030 [nucl-th/9609012].

[17] N. Ishii, Phys. Lett. **B431** (1998) 1.

[18] M. Oettel, "Baryons as Relativistic Bound States of Quark and Diquark", Ph. D. Thesis, Tübingen University, 2000, http://w210.ub.uni-tuebingen.de/dbt/volltexte/2000/177 [nucl–th/0012067].

[19] S. Mandelstam, Proc. Roy. Soc. **233** (1955) 248.

[20] J. I. Skullerud and A. G. Williams, e–print hep-lat/0007028.

[21] M. Hess, F. Karsch, E. Laermann and I. Wetzorke, Phys. Rev. **D58** (1998) 111502 [hep-lat/9804023].

[22] M. Q. Tran *et al.* [SAPHIR Collaboration], Phys. Lett. **B445** (1998) 20.

[23] J. S. Ball and T. Chiu, Phys. Rev. **D22** (1980) 2542.

[24] R. Alkofer *et al.*, proceedings of the XVth Particles and Nuclei International Conference (PANIC '99), 10 - 16 June 1999, Uppsala University, eds.: S. Kullander, G. Fäldt and B. Höistad, Nucl. Phys. **A663 & 664** (2000) 683c;
M. Oettel *et al.*, Proceedings of the Workshop on "Effective Theories of Low Energy QCD", Coimbra, Portugal, Sep. 10-15 1999; eds.: A. H. Blin et al, AIP Conference

Proceedings 508, American Institute of Physics, New York 2000, p. 73;

R. Alkofer *et al.*, Proceedings of the Eighth International Symposium on Meson-Nucleon Physics and the Structure of the Nucleon (MENU99), Zuoz, Engadine, Switzerland August 15-21, 1999; πN Newsletter **15** (1999) 238;

S. Ahlig *et al.*, Proceedings of the 21st International School of Nuclear Physics, Erice, Italy, Sep. 17-25 1999; Prog. Part. Nucl. Phys. **44** (2000) 361;

R. Alkofer *et al.*, proceedings of the Conference "Quark Nuclear Physics 2000", Adelaide, Feb. 21 - 25, 2000, Nucl. Phys. **A680** (2001) 70.

[25] G. Höhler, E. Pietarinen, I. Sabba Stefanescu, F. Borkowski, G. G. Simon, V. H. Walther and R. D. Wendling, Nucl. Phys. **B114** (1976) 505.

[26] M. K. Jones *et al.* [Jefferson Lab Hall A Collaboration], Phys. Rev. Lett. **84** (2000) 1398 [nucl-ex/9910005].

[27] I. Passchier *et al.*, Phys. Rev. Lett. **82** (1999) 4988 [nucl-ex/9907012].

[28] M. Ostrick *et al.*,A Phys. Rev. Lett. **83** (1999) 276.

[29] T. E. Ericson, B. Loiseau and A. W. Thomas, e–print hep-ph/0009312.

[30] R. G. Timmermans, T. A. Rijken and J. J. de Swart, Nucl. Phys. **A585** (1995) 143c.

[31] R. A. Adelseck and B. Saghai, Phys. Rev. **C42** (1990) 108.

[32] R. A. Adelseck and B. Saghai, Phys. Rev. **C45** (1992) 2030.

[33] R. Machleidt, K. Holinde and C. Elster, Phys. Rept. **149** (1987) 1.

[34] T. Meissner, Phys. Rev. **C52** (1995) 3386 [nucl-th/9506030].

[35] M. T. Jeong and I. T. Cheon, Eur. Phys. J. **A4** (1999) 357.

[36] R. Bilger et al., Phys. Lett. **B420** (1998) 217.

[37] F. Balestra *et al.* [DISTO Collaboration], Phys. Rev. Lett. **83** (1999) 1534 [nucl-ex/9906011].

[38] J. M. Laget, Phys. Lett. **B259** (1991) 24.

[39] A. Sibirtsev, K. Tsushima, W. Cassing and A. W. Thomas, e–print nucl-th/0004022.

[40] Z. Liang and C. Boros, Phys. Rev. Lett. **79** (1997) 3608 [hep-ph/9708488].

[41] C. Carimalo, J. Math. Phys. **34** (1993) 4930.

[42] I. R. Afnan and A. W. Thomas, "Fundamentals Of Three Body Scattering Theory," *In *Topics In Current Physics, Vol.2*, Berlin 1977, 1-47*

[43] N. Ishii, W. Bentz and K. Yazaki, Nucl. Phys. **A587** (1995) 617.

[44] C. H. Llewellyn-Smith, Ann. Phys. **53** (1969) 521.

[45] P. Maris, C. D. Roberts and P. C. Tandy, Phys. Lett. **B420** (1998) 267 [nucl-th/9707003].

[46] R. Delbourgo and M. D. Scadron, J. Phys. G **G5** (1979) 1621.

[47] C. D. Roberts, Nucl. Phys. **A605** (1996) 475 [hep-ph/9408233].

[48] P. Maris and C. D. Roberts, Phys. Rev. **C56** (1997) 3369 [nucl-th/9708029].